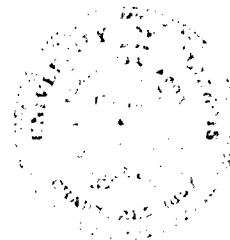DEPARTMENT OF MECHANICAL
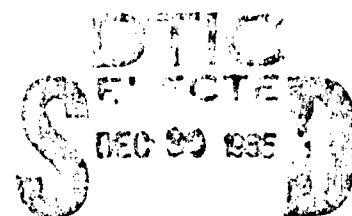AND INDUSTRIAL ENGINEERING
UNIVERSITY OF ILLINOIS AT URBANA-CHAMPAIGN
URBANA, IL 61801

UILU ENG 85-4007

Final Technical Report

PREDICTION OF DETONATION TRANSITION IN
POROUS EXPLOSIVES FROM RAPID COMPRESSION LOADINGS

DTIC
ELECTE
DEC 30 1985

D

Herman Krier and James R. Stewart

September 1985

20030117060

ANNUAL TECHNICAL REPORT

UILU-ENG-85-4007

PREDICTION OF DETONATION TRANSITION IN
POROUS EXPLOSIVES FROM RAPID COMPRESSION LOADINGS

prepared by

Herman Krier[1] and James R. Stewart[2]

Department of Mechanical and Industrial Engineering
University of Illinois at Urbana-Champaign
1206 West Green Street
Urbana, IL 61801

September 1985

---

[1]Principal Investigator; Professor of Mechanical Engineering.

[2]Graduate Research Assistant.

SECURITY CLASSIFICATION OF THIS PAGE

AD-A161 767

REPORT DOCUMENTATION PAGE

1a. REPORT SECURITY CLASSIFICATION	1b. RESTRICTIVE MARKINGS
Unclassified	None

2a. SECURITY CLASSIFICATION AUTHORITY	3. DISTRIBUTION/AVAILABILITY OF REPORT
	Approved for Public Release, Distribution Unlimited
2b. DECLASSIFICATION/DOWNGRADING SCHEDULE	

4. PERFORMING ORGANIZATION REPORT NUMBER(S)	5. MONITORING ORGANIZATION REPORT NUMBER(S)
UILU-ENG-85-4007	AFOSR-TR. 85-1134

6a. NAME OF PERFORMING ORGANIZATION	6b. OFFICE SYMBOL (If applicable)	7a. NAME OF MONITORING ORGANIZATION
University of Illinois	UIUC	Air Force Office of Scientific Research

6c. ADDRESS (City, State and ZIP Code)	7b. ADDRESS (City, State and ZIP Code)
Department of Mechanical and Industrial Eng. 1206 W. Green St., Urbana, IL 61801	ATTN: Dr. Robert J. Barker/NP Bolling AFB, DC 20332

8a. NAME OF FUNDING/SPONSORING ORGANIZATION	8b. OFFICE SYMBOL (If applicable)	9. PROCUREMENT INSTRUMENT IDENTIFICATION NUMBER
Air Force Office of Sci. Res.	AFOSR	Grant No. AFOSR-81-0145

8c. ADDRESS (City, State and ZIP Code)	10. SOURCE OF FUNDING NOS.			
AFOSR, Dr. R. J. Barker Bolling AFB, DC 20332	PROGRAM ELEMENT NO.	PROJECT NO.	TASK NO.	WORK UNIT NO.
	61102F	2301	A6	

11. TITLE (Include Security Classification)
Prediction of Detonation Transistion in Porous-Loading Explosives from Rapid Compression Loading

12. PERSONAL AUTHOR(S)
Herman Krier and James R. Stewart

13a. TYPE OF REPORT	13b. TIME COVERED	14. DATE OF REPORT (Yr., Mo., Day)	15. PAGE COUNT
Final Report	FROM 30Aug83 TO 10Sep85	15 September 1985	61

16. SUPPLEMENTARY NOTATION

17.	COSATI CODES		18. SUBJECT TERMS (Continue on reverse if necessary and identify by block number)
FIELD	GROUP	SUB. GR.	Detonation Transition of Explosives, Analysis of Shock Initiation; Porous Explosive

19. ABSTRACT (Continue on reverse if necessary and identify by block number)

Increasing the nitramine content of solid rocket propellants increases the overall performance of the system as well as the sensitivity to Shock to Detonation Transition (SDT) and Deflagration to Detonation Transition (DDT). This report deals primarily with the analysis and numerical modeling of a combined SDT/DDT event. The results show that in some instances a zone of burning granulated propellant, confined and adjacent to a zone of cast propellant, can provide a rapid enough pressure-rise rate to shock initiate the cast material. This type of detonation hazard scenario is a real possibility in any high-energy rocket motor environment.

The modeling study also indicates areas where important assumptions need to be further researched. These include: (a) relations for dynamic (transient) collapse of the voids or pores; (b) relations for setting the volume percent of hot spots based on initial porosity; (c) the evaluation and expression for the chemical rate of decomposition of the reactive, shocked material; and (d) the assessment of two-phase mixture equilibrium.

20. DISTRIBUTION/AVAILABILITY OF ABSTRACT	21. ABSTRACT SECURITY CLASSIFICATION
UNCLASSIFIED/UNLIMITED ☒ SAME AS RPT. ☐ DTIC USERS ☐	Unclassified

22a. NAME OF RESPONSIBLE INDIVIDUAL	22b. TELEPHONE NUMBER (Include Area Code)	22c. OFFICE SYMBOL
Dr. Robert J. Barker	202-767-5011	AFOSR/NP

Block No. 19 Continued.

"The predicted run-to detonation distance as a function of porosity for HMX explosive compares favorably with limited shock initiation experiments. There is no data available to check whether the predictions of ramp-wave compressions (where rise times exceed several microseconds) presented here are valid.

Accesion For		
NTIS CRA&I	☑	
DTIC TAB	☐	
U. announced	☐	
Justification		
By		
Distribution /		
Availability Codes		
Dist	Avail and/or Special	
A-1		

TABLE OF CONTENTS

ABSTRACT

Increasing the nitramine content of solid rocket propellants increases the overall performance of the system as well as the sensitivity to Shock to Detonation Transition (SDT) & Deflagration to Detonation Transition (DDT). This report deals primarily with the analysis and numerical modeling of a combined SDT/DDT event. The results show that in some instances a zone of burning granulated propellant, confined and adjacent to a zone of cast propellant, can provide a rapid enough pressure-rise rate to shock initiate the cast material. This type of detonation hazard scenario is a real possibility in any high-energy rocket motor environment.

The modeling study also indicates areas where important assumptions need to be further researched. These include: (a) relations for dynamic (transient) collapse of the voids or pores; (b) relations for setting the volume percent of hot spots based on initial porosity; (c) the evaluation and expression for the chemical rate of decomposition of the reactive, shocked material; and (d) the assessment of two-phase mixture equilibrium.

The predicted run-to detonation distance as a function of porosity for HMX explosive compares favorably with limited shock initiation experiments. There is no data available to check whether the predictions of ramp-wave compressions (where rise times exceed several microseconds) presented here are valid.

LIST OF SYMBOLS

a_0	initial pore radius (μm)
C_v	specific heat (erg/g/K)
d	particle diameter (cm)
e	specific internal energy (erg/g)
E	total energy
E*	activation energy (erg/mole)
m	mass (g)
L	bed length (cm)
L_{SDT}	detonation run-up length (cm)
P	stress (dynes/cm^2)
P*	maximum axial stress (dynes/cm^2)
Q	chemical energy release rate (erg/g/s)
R	gas constant (erg/g/K)
$\bar{R}$	universal gas constant
t	time (s)
t*	characteristic rise time (s)
T	temperature (K)
u	particle velocity (cm/s)
v	specific volume (cm^3/g)
V	volume (cm^3)
W	decomposed mass fraction
x	spatial location (cm)
Z	frequency factor (1/s)

Greek

α	$V_T/V_S = 1/(1-\phi)$
β	covolume (cm^3/g)
Γ	Gruneisen coefficient
ϕ	porosity, V_g/V_T
ρ	density (g/cm^3)
ψ	Helmholtz free energy (erg/g)
τ	dynamic compaction model relaxation constant (μsec)

Subscripts

CJ	Chapman-Jouguet state
i	isentrope
g	gas
H	hot spot
o	initial state
x	$\partial()/\partial x$
s	solid
t	$\partial()/\partial t$

CHAPTER I
TRANSITiON TO DETONATION: THE MODEL

Introduction

In 1984 a model was developed yielding preiiminary results that predicted the processes of transition to detonation by ramp-wave compression of porous explosives [1]. This report highlights the major features of this model and presents additional analysis which we believe indicates that the physical and chemical processes in the model are properly described.

Predicting Deflagration to Detonation Transition (DDT) depends on being able to prescribe the shock loading conditions, i.e. the rate at which an explosive is compressed. An actual shock loading condition represents sub-microsecond rise times, while ramp-wave loadings could compress the solid in relatively long times, exceeding tens of microseconds.

The motivation of our work is to assess the hazard of DDT in high energy solid propellant rocket motors. Data and analysis indicate that sufficient porosity in the propellant is necessary. Thus in order for a DDT to occur in a full-scale motor, the grain must first be damaged. This has been demonstrated in the laboratory many times when small-scale (20 to 40 cm) packed beds of granulated propellant undergo the transition from deflagration to detonation. Combustion of the high surface-to-volume ratio micron-sized fragments provides the rapid pressurization rate necessary to shock initiate the remaining fragments. By increasing the nitramine content of the propellant mixture, the propensity to detonate is increased in two ways: the decomposition rate of the propellant increases and the shock sensitivity increases. Although little has been done to experimentally verify it, one can also assume that the particle morphology (size, shape, and surface roughness) greatly influences the decomposition rate and thus the build up to detonation.

We have proposed two possible methods whereby DDT can occur in a solid rocket motor. In the first case a length, L, of the motor grain is completely fragmented. This case was the topic of several research papers [2-4] by our group and will be discussed here only to provide a comparison with the second case proposed. In Case 1, the bed is of sufficient length to allow the transition to detonation to occur within the granulated material, that is, $L > L_{SDT}$ where L_{SDT} is the detonation run-up length measured from the ignition

source. In Case 2, $L < L_{SDT}$ and the detonation occurs in the upstream cast material. However in both cases, the confined burning of the propellant fragments is what drives the deflagration wave to a high-order detonation. The reader should consult Ref. [5] for a general overview of DDT in different propellants and explosives and Ref. [6] for typical experimental results.

In Case 1, the length of the packed bed is longer than the critical length necessary for accelerated convective combustion to occur, and subsequent detonation is inevitable. Figure 1 illustrates the Case 1 bed configuration. The second DDT scenario involves a region of burning granulated propellant providing the impetus to shock initiate an adjacent region of the case propellant. This is illustrated in Fig. 2. The cast material (Zone 1) can contain "blind" pores and is assumed to be impermeable to the flow of hot gases from the zone of fragmented material (Zone 2). This implies that, unlike the first DDT scenario discussed, only stress waves can be transmitted across the Zone 1/Zone 2 interface. Figure 3 is a schematic representation of the sequence of events leading to this type of DDT. Superimposed on each section of the figure is a solid line representing the local gas porosity (volume of gas/total volume) as a function of x, the bed location. A value of ϕ equal to unity represents a zone of all gas while ϕ equal to zero indicates a voidless solid.

Part A shows a zone of burning granular propellant adjacent to a zone of porous, cast propellant. Here, the heavy black dots are representative of microvoids in the cast material. Illustrated in Part B is the collapse of the pores, a result of the stress load transmitted across the granulated bed/cast propellant interface. Parts C and D show the length of the pore collapse zone to increase with time as the lead compression waves travel farther into the propellant bed. The finite compression waves coalesce into a shock front which subsequently shock initiates the cast propellant at a location ℓ_{CJ} ahead of the interface. From this location a detonation wave propagates through the porous material while a retonation wave propagates back through the compressed material (Part E).

In related research, Setchell [7] studied ramp-wave initiation mechanisms using waves with rise-times of 0.3 to 0.8 μs. In Ref. [7] the ramp-waves were developed by propagation of an impact-generated shock wave through a unique material which has the property of spreading out the shock front into a ramp-
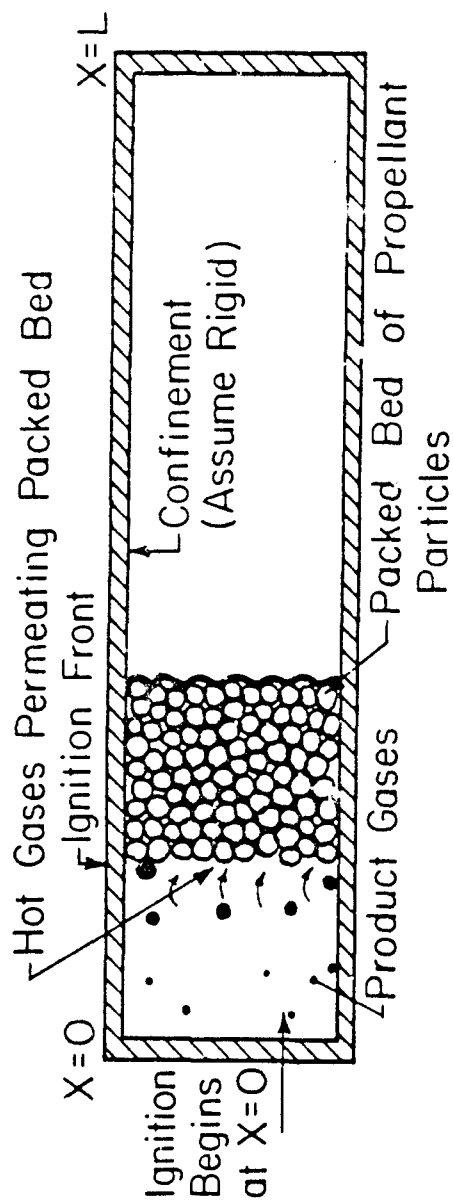
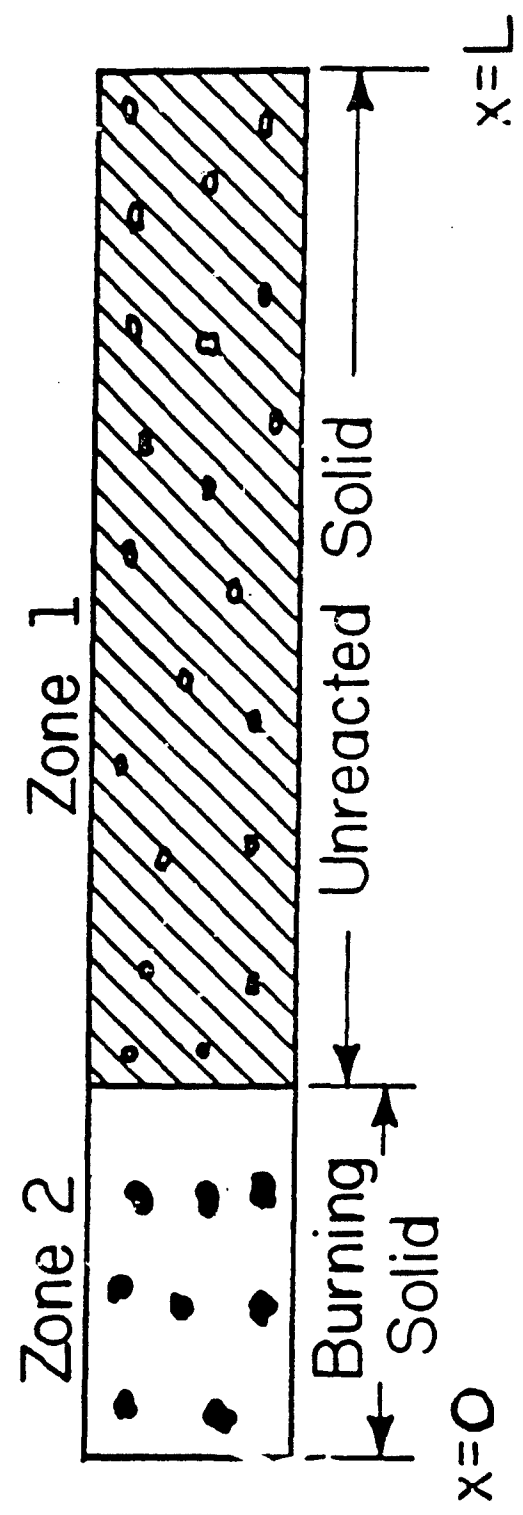Figure 1   Enlargement of granulated bed showing processes that need to be modeled for DSDT.

Figure 2 Sketch of the two assumed regions necessary to provide DSDT. The model developed here attempts to describe the dynamic processes in Zone 1 with pressure loading occurring at the interface between Zone 1 and Zone 2.

(A) Ignition

$\phi(X)$

Porous Material
Ignition

(B) Convective Flame Spreading

Burning Zone

(C) Pore Collapse

Leading Compression Wave
Pore Collapse

(D) Plug Formation

Plug

(E) Shock Formation

Plug
Shock

(F) Shock Initiation (Detonation)
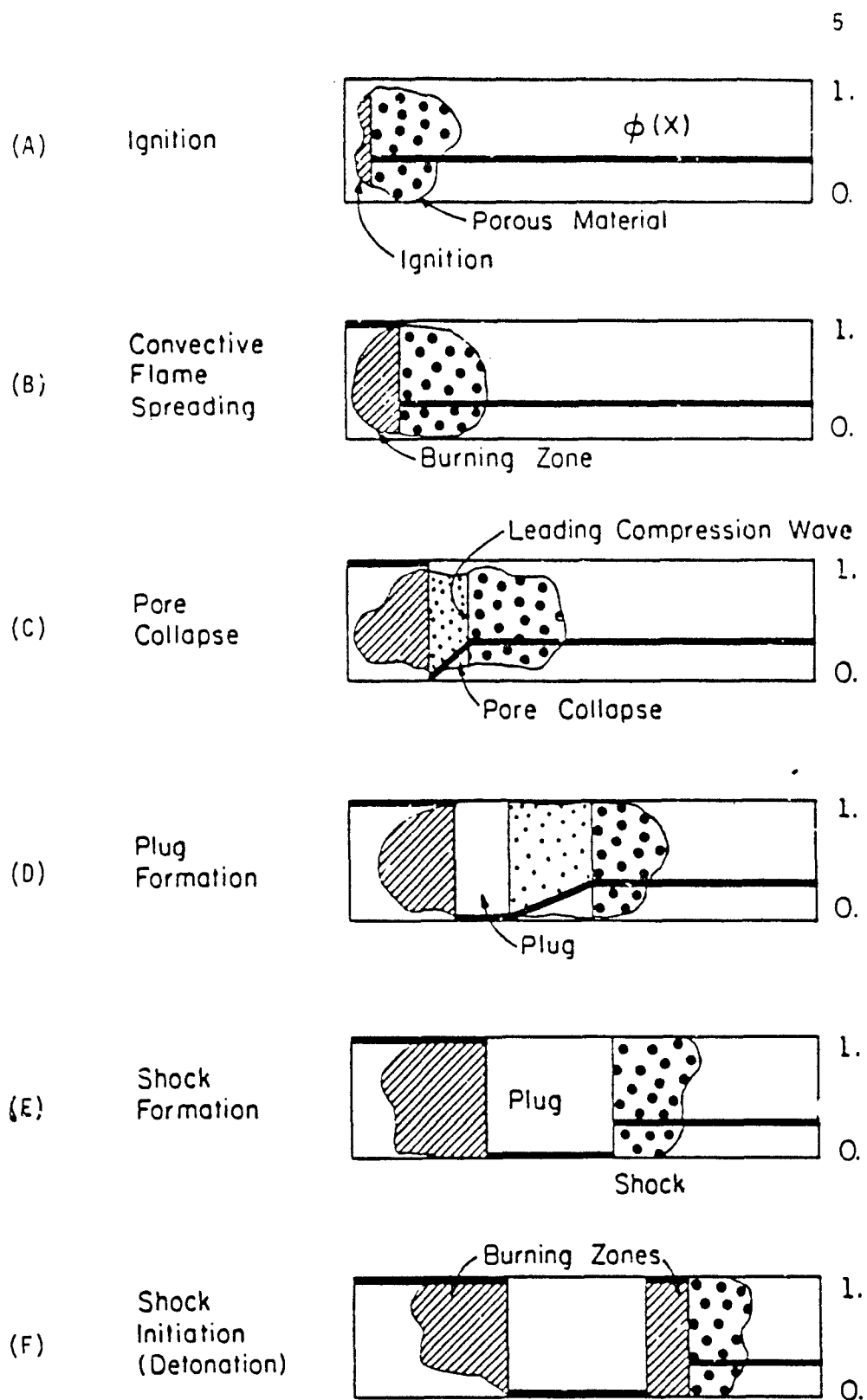
Burning Zones

Figure 3   Proposed six-part sequence of events leading to DSDT.

wave. In the work presented here, the rise-times were much longer than those cited in [9], typically of the order of tens of microseconds. These slower rise-times are typical pressure-time histories generated within a deflagrating bed of granular HMX.

The purpose of this work is to model the key elements of the six-part scenario shown in Fig. 3. A one-dimensional hydrodynamic Lagrangian finite difference technique is used to numerically solve the conservation equations. A static pore collapse model [8] which demarcates three regimes of deformation—elastic, elastic-plastic, and plastic—is utilized to determine the rate of compaction and the development of the solid plug. Chapter 3 investigates two dynamic pore collapse models. Furthermore, a hot spot model [9] is incorporated in the code to define the sensitivity to reaction. By introducing reactive chemistry to the code, a strong effort is made to model the detonation and retonation waves which are initiated by a shock wave generated from ramp-wave inputs with rise times on the order of tens of microseconds. It was shown in Ref. [1] that rise times, t*, of this order are typical for burning, granulated beds which have lengths less than their critical detonation run-up length.

The Model

The scope of the work presented in this report is to model DDT in the granulated bed/cast propellant configuration shown in Fig. 2. It is assumed that the granulated bed is not long enough (L < L_{SDT} to undergo DDT in the usual sense (Case 1) but, by convective burning, can provide the driving force necessary to shock initiate the upstream cast propellant. For this analysis the cast propellant is assumed to have "blind" pores and to be impermeable to the flow of product gases generated in the granular bed. This implies that only stress waves can be transmitted across the granular bed/cast propellant interface. The rate at which the reacting granulated bed stresses the cast propellant is a function of many of the granular bed parameters including particle size, loading density, solid density, and reaction rate. In the analysis to follow, the boundary pressure-rise rate was determined by executing the DDT code discussed in Ref. [3] for granular beds with lengths, L, less than the detonation run-up length and recording the pressure-rise rate at the end opposite the igniter. The pressurization rate in the granular bed, dP*/dt*, is strongly dependent on the size of the particles being consumed.

The larger the particle being consumed, the slower the pressurization rate on the interface. Thus, from this type of analysis we have been able to determine the P(t) boundary condition for the stress wave analysis of the upstream cast propellant.

The P(t) functions obtained from this modeling effort have been linearized for this work and are expressed as

$$P(t) = (P^*-P_0)(t/t^*)+ P_0 \qquad t \leq t^* \qquad (1.1a)$$

and

$$P(t) = P^* \qquad\qquad t \leq t^* \qquad (1.1b)$$

where P* is the maximum stress in the bed. The parameter t* is a characteristic rise-time for the ramp-wave input function.

The Lagrangian or material form of the governing equations are incorporated in the hydrodynamic analysis of a continuous material with a moving boundary. In the problem addressed, the moving boundary is a result of the applied stress load from the burning granulated bed. The one-dimensional unsteady form of the conservation of mass, momentum, and energy equations are expressed for the two-phase mechanical mixture as

$$v_t = vu_x, \qquad (1.2)$$
$$u_t = -vP_x, \qquad (1.3)$$

and

$$e_t = -Pv_t + Q. \qquad (1.4)$$

In the above expressions, v represents the specific volume of the mixture; u, the particle velocity; e, the specific internal energy; P, the total stress; and Q, the heat added per unit mass per unit time. The subscripts x and t indicate partial derivatives with respect to the Lagrangian spatial coordinate and time, respectively. In addition to the conservation equations, a material equation of state, P = P(v,e), and appropriate constitutive relations provide for mathematical closure.

For the solid material the equation of state $P_s(v_s,e_s)$ and the caloric equation $e_s(v_s,T_s)$ are expressed in terms of a Helmholtz free energy function [10], $\psi(v_s,T)$, and its thermodynamic derivatives through the Second Law of Thermodynamics reciprocity relations

$$P_s = - (\partial\psi/\partial v_s)_T \qquad (1.5)$$

$$e_s = \psi - T_s (\partial\psi/\partial T_s)_V . \qquad (1.6)$$

With the assumption that the Gruneisen coefficient is constant, the Helmholtz free energy function takes the form

$$\psi = J(v_s) + \Gamma C_{vs} \ln(v_0/v_s)(T_s-T_0) + C_{vs}[T_s \ln(T_0/T_s) + T_s-T_0] \qquad (1.7)$$

where Γ is the Gruneisen coefficient defined by the thermodynamic derivative

$$\Gamma(v) = - v \left(\frac{\partial P}{\partial e}\right)_V \qquad (1.8)$$

and C_{vs} is the specific heat at constant volume of the solid phase

$$C_{vs} = \left(\frac{\partial e}{\partial T}\right)_V . \qquad (1.9)$$

The term $J(v_s)$ in Eq. (1.7) is a nonlinear volume-dependent function determined from shock Hugoniot experiments [10].

With the introduction of product gases into the system, a constitutive law for the gas phase must also be provided. A non-ideal covolume equation of state is utilized

$$P_g = \rho_g R T_g (1 + \beta\rho_g) \qquad (1.10)$$

where R is the gas constant and β is a covolume correction term. The value of β is determined from the values for pressure, temperature, and density at the CJ state predicted by the TIGER code [11]. Table 1 gives a listing of those values for several loading densities of HMX. In accordance with the reciprocity relations defined earlier (Eqs. (5) and (6)), the caloric equation of state for the gas phase is

$$de_g = C_{vg} dT_g \qquad (1.11)$$

where C_{vg} is the specific heat at constant volume of the product gases.

Table 1 CJ Parameters (P,T,v,D, from Tiger)

α_0	P_{CJ} (GP$_a$)	T_{CJ} (K)	v_{CJ} (cc/g)	D (mm/μs)	β (cc/g)
1	36.57	3840	0.4067	9.20	4.86
1.06	32.25	3973	0.4260	8.77	4.50
1.12	28.50	4083	0.4471	8.36	4.22
1.19	25.20	4171	0.4707	7.98	4.00
1.27	22.22	4280	0.5276	7.33	3.74
1.46	17.26	4304	0.5629	7.05	3.68

The governing equations (Eqs. (2) through (4)) are expressed in terms of the thermodynamic properties (P,v,e) and dynamic variable u of the two-phase mixture. The individual phase volumes sum to equal the total $V_T = V_S + V_g$ where $V_i = v_i m_i$ (i = g,s). Likewise for the mixture total energy $E_T = E_G + E_S$.

We define the material porosity (α) as the ratio of total volume to volume occupied by the solid phase

$$\alpha = V_T/V_s \qquad (1.12)$$

and incorporate a three-step static material collapse model [8]. Current work by our research group involves an investigation of the more realistic dynamic material response models.

A first order Arrhenius burn model is used to describe the chemical decomposition of the reactive material

$$\frac{dW}{dt} = -ZW \exp(-E^*/\bar{R}T^*) . \qquad (1.13)$$

In the above equation, W is the mass fraction of unreacted explosive, $W = m_s/m_{so}$; Z is the frequency factor, E^* the activation energy, $\bar{R}$ the universal gas constant, and T^* the characteristic burn temperature. During compression of the porous bed, T^* represents a "hot spot" temperature due to irreversible heating at pore sites. The localized hot spot temperature is different from the bulk shock temperature and is calculated from an energy partition model [9]. The underlying assumption in this hot-spot model is that the shocked porous material is at one of two possible temperatures, a bulk shock temperature, T, or a hot spot temperature, T_H. The energy deposited by the shock wave is equated on a mass fraction basis to the sum of the reversible work done in isentropically compressing the bulk of the material plus the irreversible heating of localized hot spots [9]

$$\frac{P+P_0}{2} (v_{to}-v) = W_H e(v,T_H) + (1-W_H)e_i(P) . \qquad (1.14)$$

In Eq. (1.14), the left-hand side represents the total energy deposited in the material by the shock of strength P. The term $e_i(P)$ represents the energy re-

quired to isentropically compress the bulk of the material to the final shock pressure and the remaining energy term, $e(v,T_H)$, is the energy available to irreversibly heat the hot spots. This model assumes the mass fraction of the hot spots, W_H, to be equal to the preshock volume fraction of pores.

$$W_H \ (v_{to}/v_{so}-1) = \alpha_0 - 1 \qquad\qquad (1.15)$$

Here, the subscript "to" represents the initial porous state and the subscript "so" refers to the homogeneous initial state. This particular macroscopic hot spot model was chosen since it is more applicable to the problem at hand. The reader should consult the literature for one of the more detailed microscopic approaches to the theory of hot spots.

Equations (1.2) through (1.15) define the fluid motion and thermodynamic state of continuous, reactive, porous media. The system of equations is solved by using a finite difference numerical technique. At $t = 0$, the bed of porous propellant is discretized into J cells labeled from left to right as $j = 1,2,....,J$. The thermodynamic properties (pressure, temperature, internal energy, and specific volume) are assumed to be constant over the width of each cell. At the boundaries between the cells, values for particle velocity and spatial location are assumed known at $t = 0$. The reader is referred to Ref. [12] for a listing of the finite difference approximations to the governing differential equations and constitutive relations.

Results

As stated earlier, the purpose of this work is to predict the transient events leading to detonation in a bed of porous, cast propellant being stress loaded at one end by a burning, granulated bed of the same material. In our preliminary calculations, we found that rise-times of $10 \ \mu s < t^* < 30 \ \mu s$ were typical of most of the granulated beds studied. Note that these are greater than those cited earlier [7].

Several cases with various maximum input stresses, characteristic rise times, and initial porosities were chosen to test the trends of the computer model. The first case considered has an initial porosity of $\alpha_0 = 1.1176$ and is initiated by a "ramp" wave with a maximum input pressure of $P^* = 2$ GPa and characteristic rise time of $t^* = 10 \ \mu sec$. Figures 4 through 6 illustrate the

distribution history of three key parameters, namely P, α, and (1-W). For this particular case, three specific segments in time were chosen for illustration purposes. The first time shown in all the three separate figures is t = 10 μsec. By viewing Fig. 4a, one can see that the compression wave has propagated into the bed to a distance of 1.5 cm. Notice even though the left boundary has reached the maximum input stress shown approximately at a location of 2 mm into the bed, the shock front has not fully developed. Figure 5a illustrates the closure of the voids as a result of the compression wave. One can see from Fig. 6a (gas-phase mass fraction) that the reaction has yet to commence.

As time progresses to 12 μsec, Fig. 6b shows that the reaction has commenced. This occurrence can also be viewed by an increase in porosity (α), as displayed in Fig. 5b at that instant. Induced by the initiation of propellant decomposition, an increase in strength of the compression front occurs, as is evident in Fig. 4b. With the increase in the degree of reaction, the chemical energy further contributes to strengthen the compression front.

At t = 13 μsec, the decomposition of the propellant is complete in a small region of the bed near x = 2 cm, as shown in Fig. 6c. The porosity distribution, displayed in Fig. 5c (at 13 μsec), shows compression ahead of the decomposition region. The net effect of all of this is a right moving detonation wave and a left (or rearward) moving retonation wave, as illustrated in Fig. 4c. Note that the retonation wave has a higher peak pressure than the detonation wave. This is due to the higher density of the material the wave is propagating through. The steady detonation wave continues to propagate even further into the bed at a predicted CJ pressure of 25 GPa and a corresponding CJ temperature of 3923 K.

In addition to the figures just presented, the locus of the stress and reaction fronts are shown in Fig. 7. The dashed line depicts the stress wave propagation into the bed, initiating the detonation at t = 12.41 μsec, x = 2.05 cm. The solid lines represent the locus of the right and left traveling detonation fronts. Figure 7 also shows the termination point of the retonation wave. A change in velocity is apparent in the left traveling wave at the termination point. The slopes of the solid lines correspond to a detonation and retonation velocity of D = 8.8 mm/μsec and R = 9.1 mm/μsec, respectively.

t=12.0 μsec

t=10.0 μsec
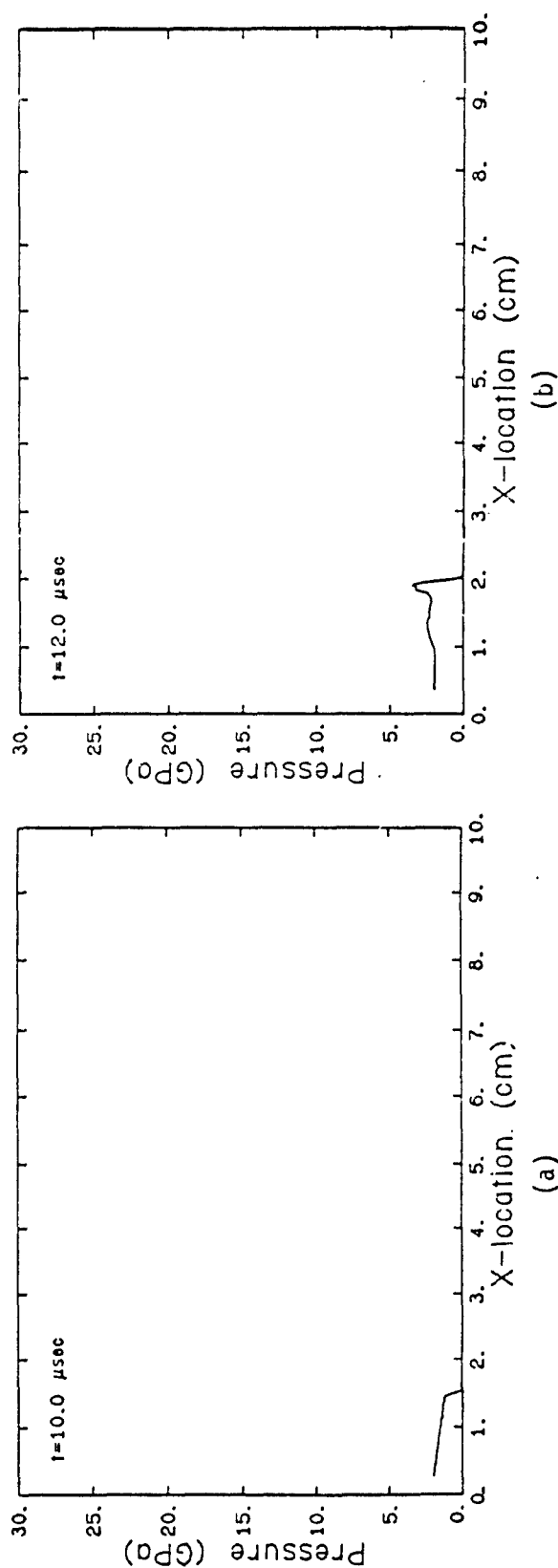
Figure 4   (a)   Pressure-distance profiles for porous HMX. Other inputs are P* = 2 GPA, t* = 10 μsec. At t = 10 μsec, no reaction is noticeable.

           (b)   At t = 12 μsec, reaction has commenced.
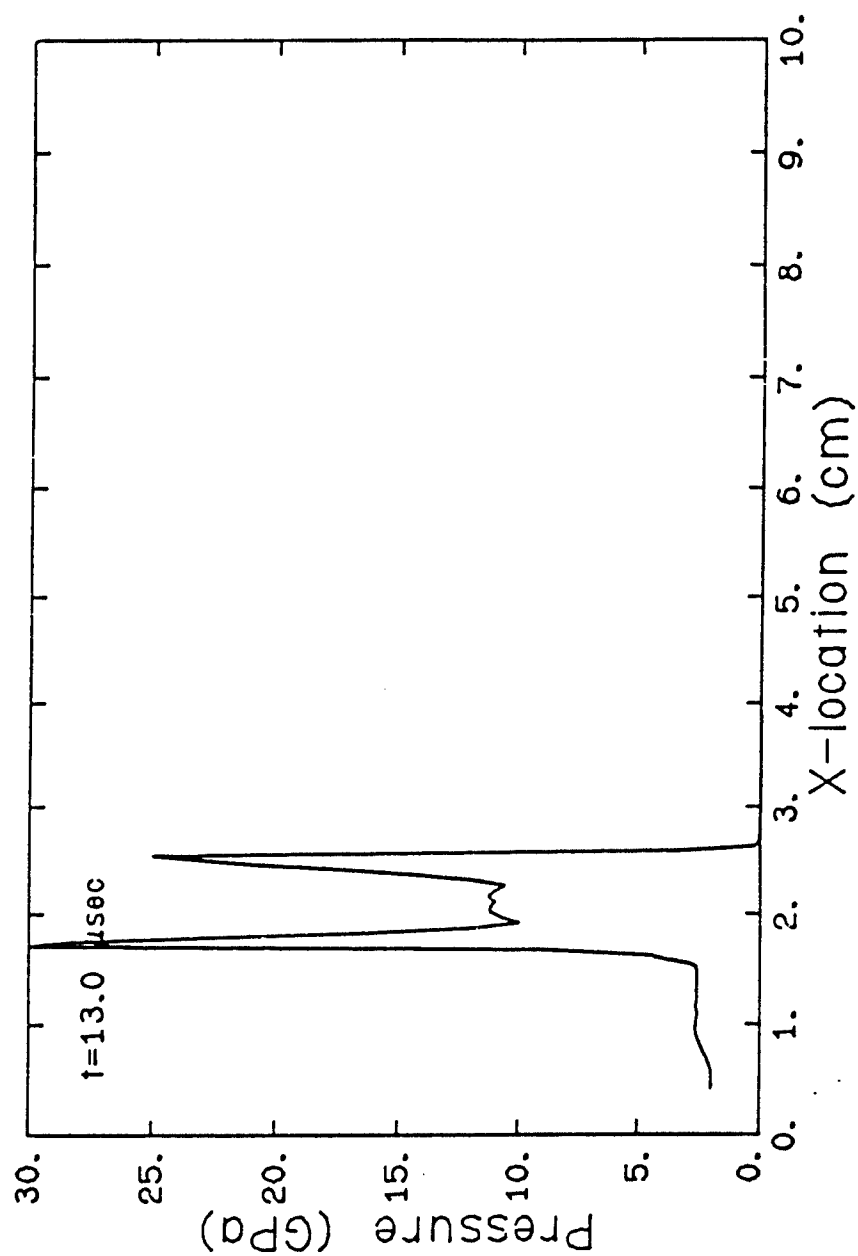
Figure 4c Pressure-distance profile at t = 13 sec showing
full reaction with P_{CJ} = 25 GPA, D = 8.8 mm/μsec.
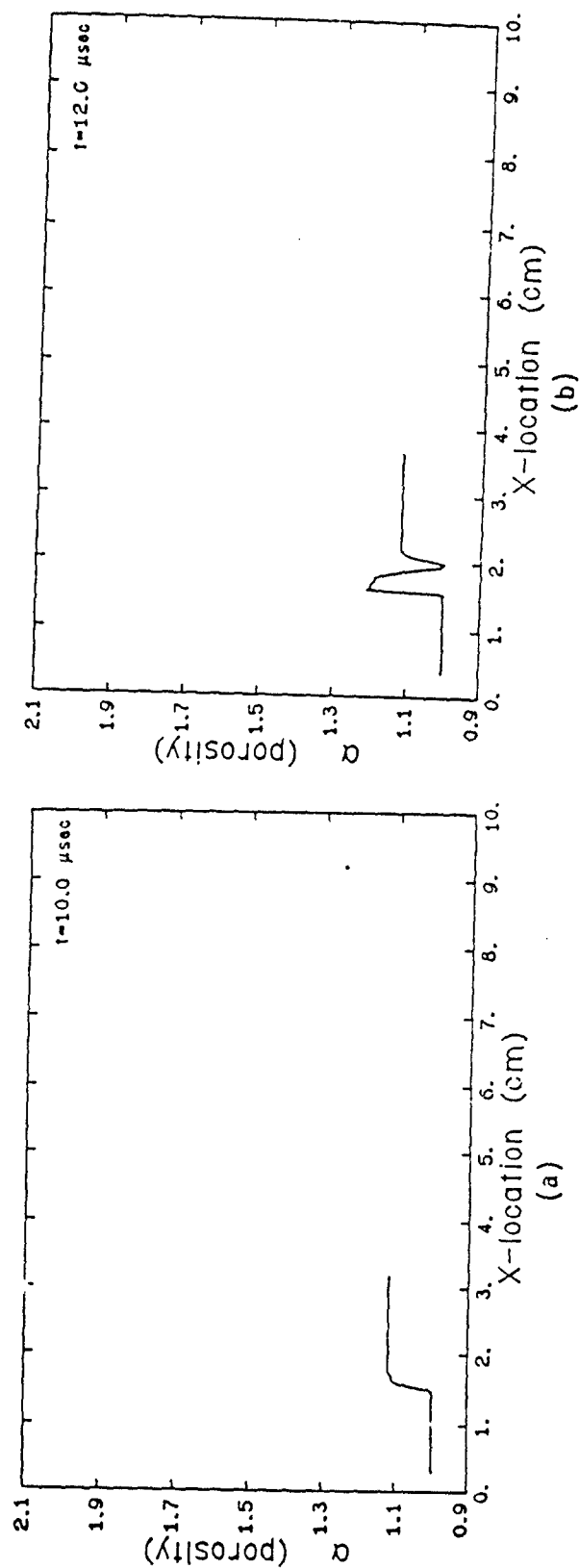
Figure 5 (a) Porosity-distance profiles for α_0 = 1.1176,
P* = 2 GPA, t* = 10 μsec. Part (a) shows
the profile at t = 10 μsec prior to detonation.
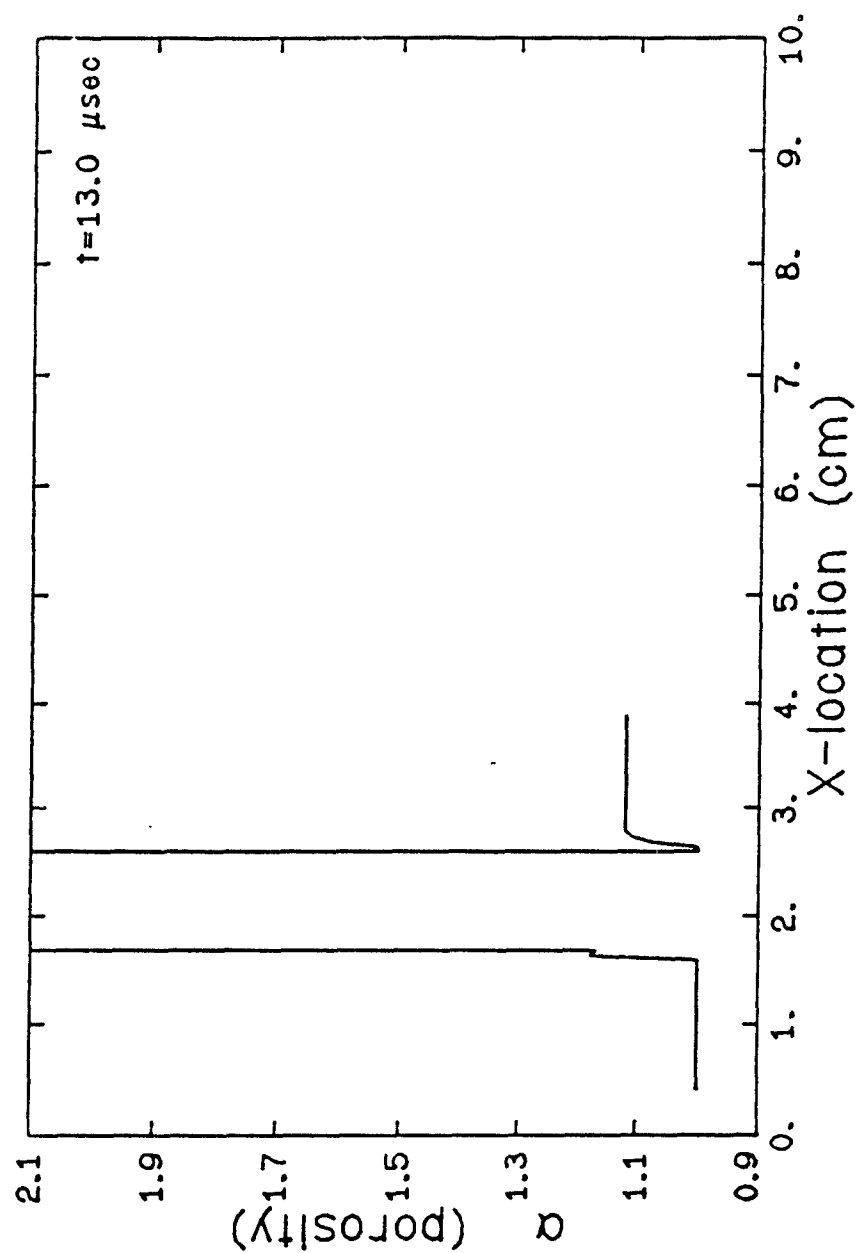(b) Part (b) shows the reaction zone development at t = 12 μsec.

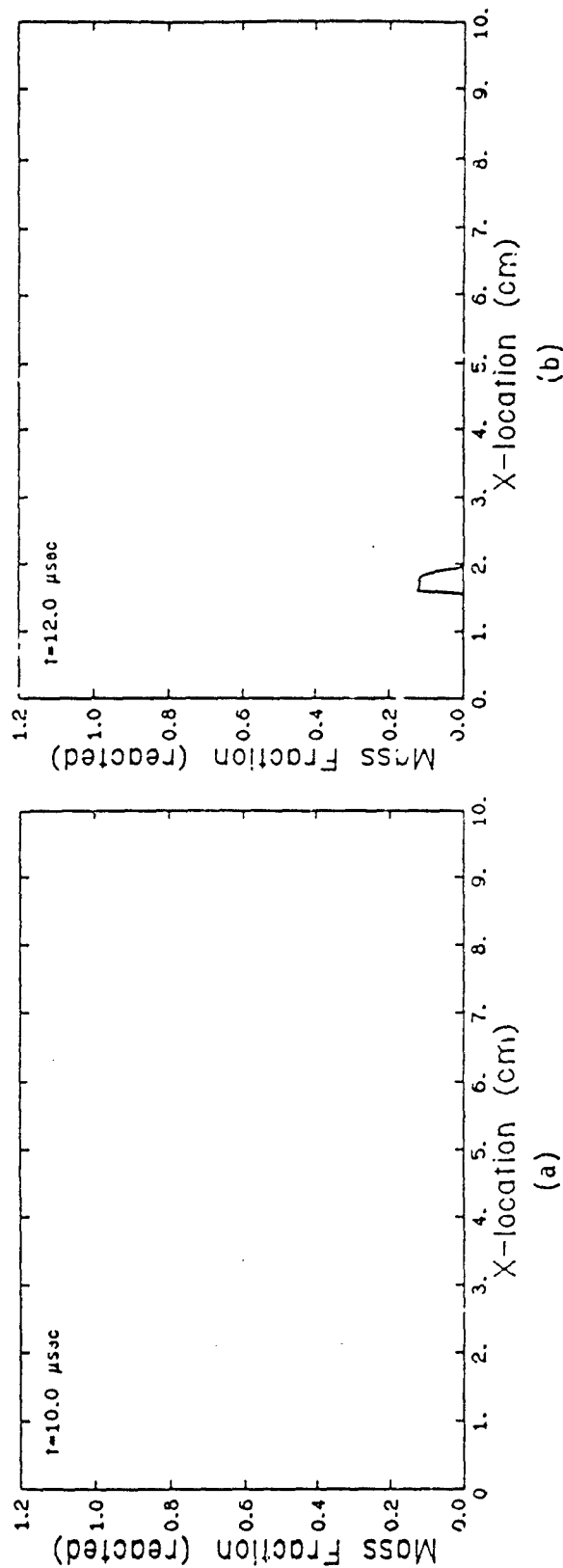Figure 5c Porosity-distance profile at t = 13 μsec showing detonated zone (1.6 < x < 2.6 cm).

Figure 6 (a) Profiles of mass fraction reacted in the explosive bed for $\alpha = 1.1176$, $P* = 2$ GPA, $t* = 10$ μsec. In (a) at $t = 10$ μsec, no reaction is noticeable.
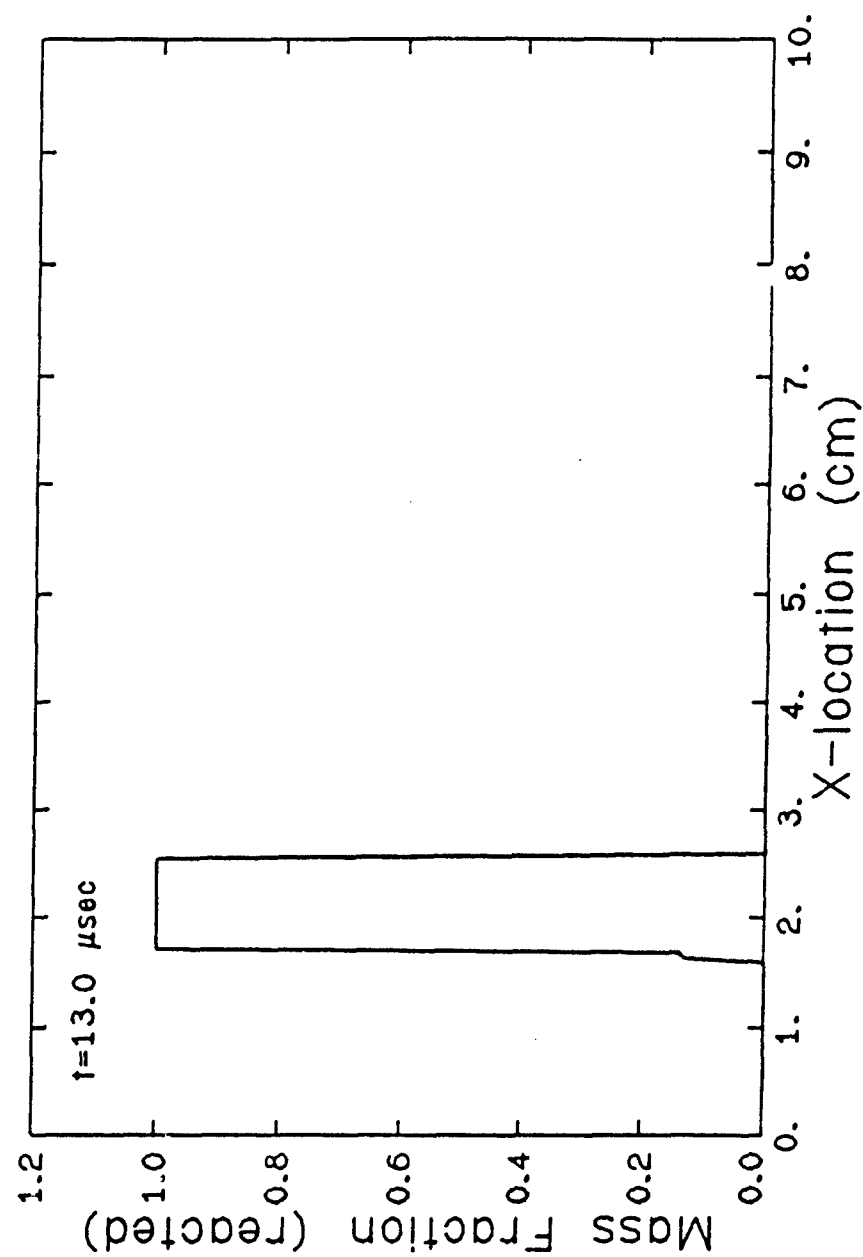
(b) In (b) at $t = 12$ μsec, reaction has commenced.

Figure 6c Profile of mass fraction reacted in the explosive
bed at t = 13 μsec showing complete detonation within
the detonated zone (1.6 < x < 2.6 cm).

The plot shows:
- Y-axis: Mass Fraction (reacted), ranging from 0.0 to 1.2
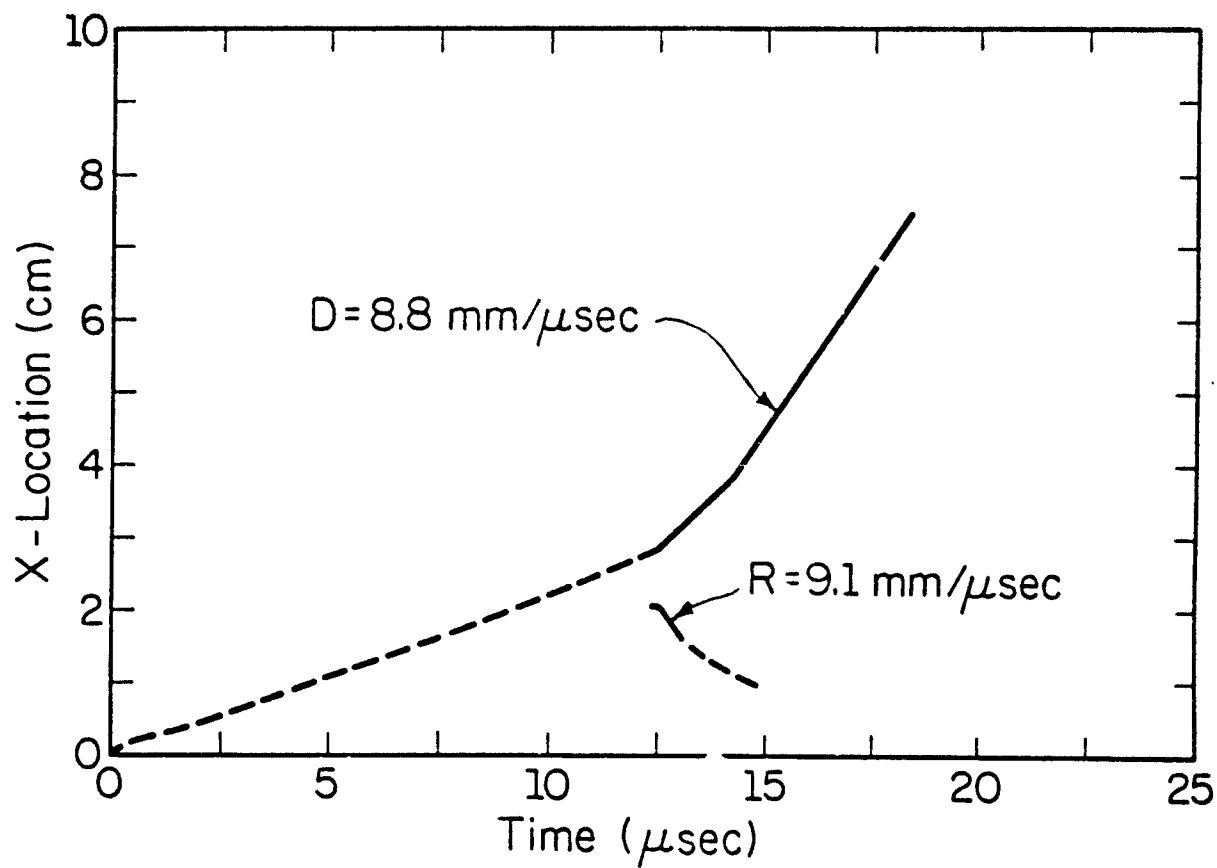- X-axis: X-location (cm), ranging from 0. to 10.
- t=13.0 μsec

Figure 7   Predicted locus of the compression front with transition
to both detonation and a rearward moving retonation
(α_0 = 1.1176, P* = 2 GPa, t* = 10 μsec).

As stated earlier in the text, the granular bed (Zone 2, Fig. 2) provides the driving force to shock initiate the cast material (Zone 1, Fig. 2). In addition, the pressure-rise rate at the Zone 1/Zone 2 interface is a function of several key parameters in the granulated bed. Figure 8 illustrates the influence of pressure-rise rate on the run-up distance to detonation, L_{SDT}. Data are presented for four different values of t* (1, 3, 5, and 10 µs, respectively). The slower rise time of 10 µs corresponds to a granular bed with d_0 = 500 µm particles driving the shock build-up process. Previous calculations show that HMX particles of this size would require a rather long bed length in order to exhibit DDT in the Case 1 situation. In general, one would expect a greater run-up distance to correspond to a longer characteristic rise time for a specific input pressure, since the compression front will reach the critical pressure needed to initiate detonation later. Indeed, Fig. 8 demonstrates the occurrence of a longer run-up distance for a longer characteristic rise time at a specific input pressure. Therefore, for low input pressures and critically long characteristic rise times, detonation is not expected to occur in a 10 cm bed, eliminating the hazard of DDT in the Case 2 configuration. In regards to the actual rocket motor configuration, this implies that the DDT Case 2 hazard does exist if the granular particles are sufficiently small and the Zone 1 bed length is greater than L_{SDT} for the corresponding dP*/dt*.

Figure 9 shows the run-up to detonation distance, L_{SDT} as a function of t*, the compression wave rise time, for two values of initial porosity, α_0. Here, the sample with the lower α_0 is observed to have a shorter run-up distance than the more porous sample. This is explained as follows. Although the higher porosity material has a larger hot spot volume (as predicted by Eq. (16)), the low porosity material has a much higher local density and thus contributes more energy to the shock front upon decomposition.
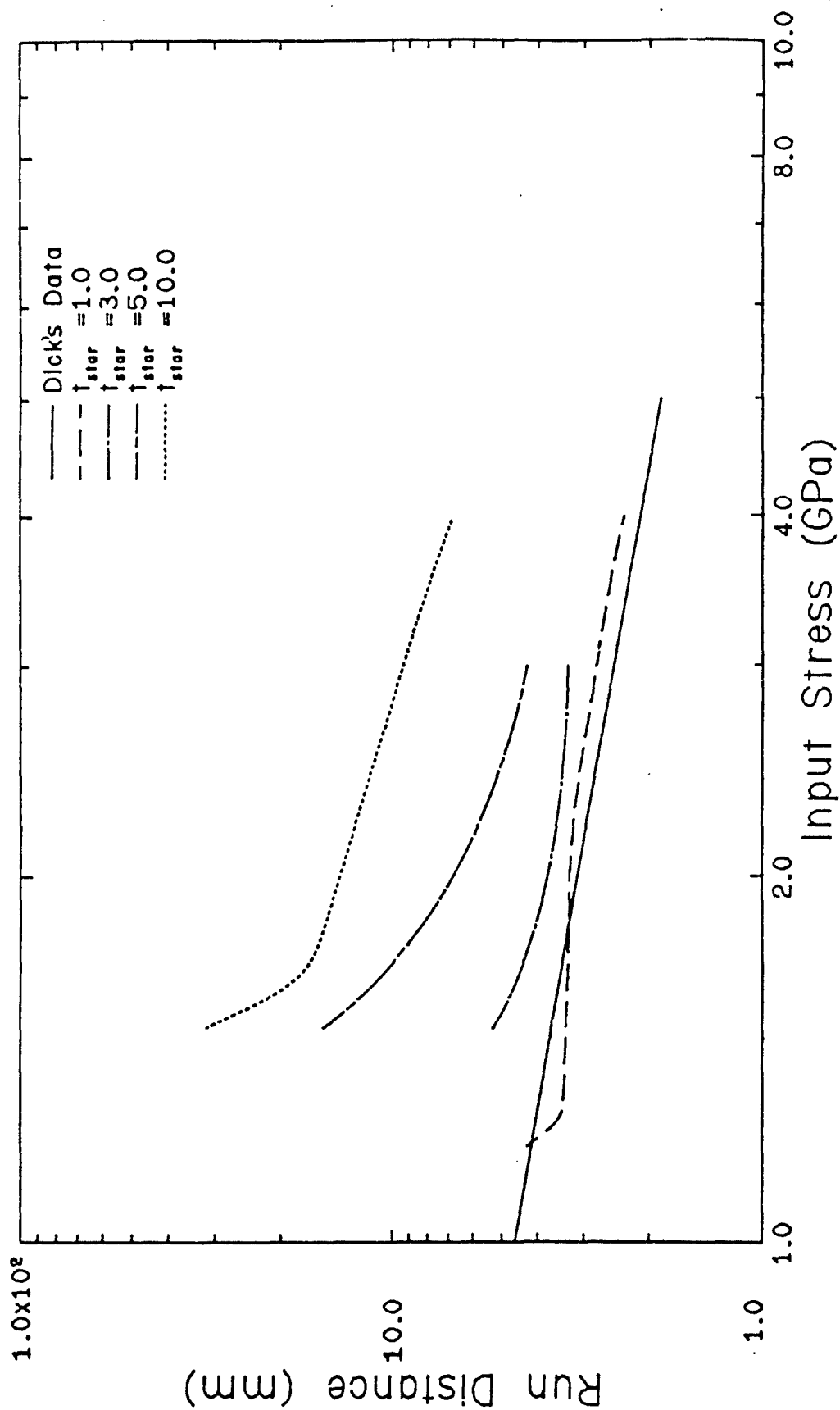
Figure 8   Prediction of run-distance to detonation vs. input maximum pressure for rise-times increasing from 1 to 10 μsec. The experimental data of J. J. Dick is shown as the solid line. Both model and data were for $\alpha_o = 1.5322$.
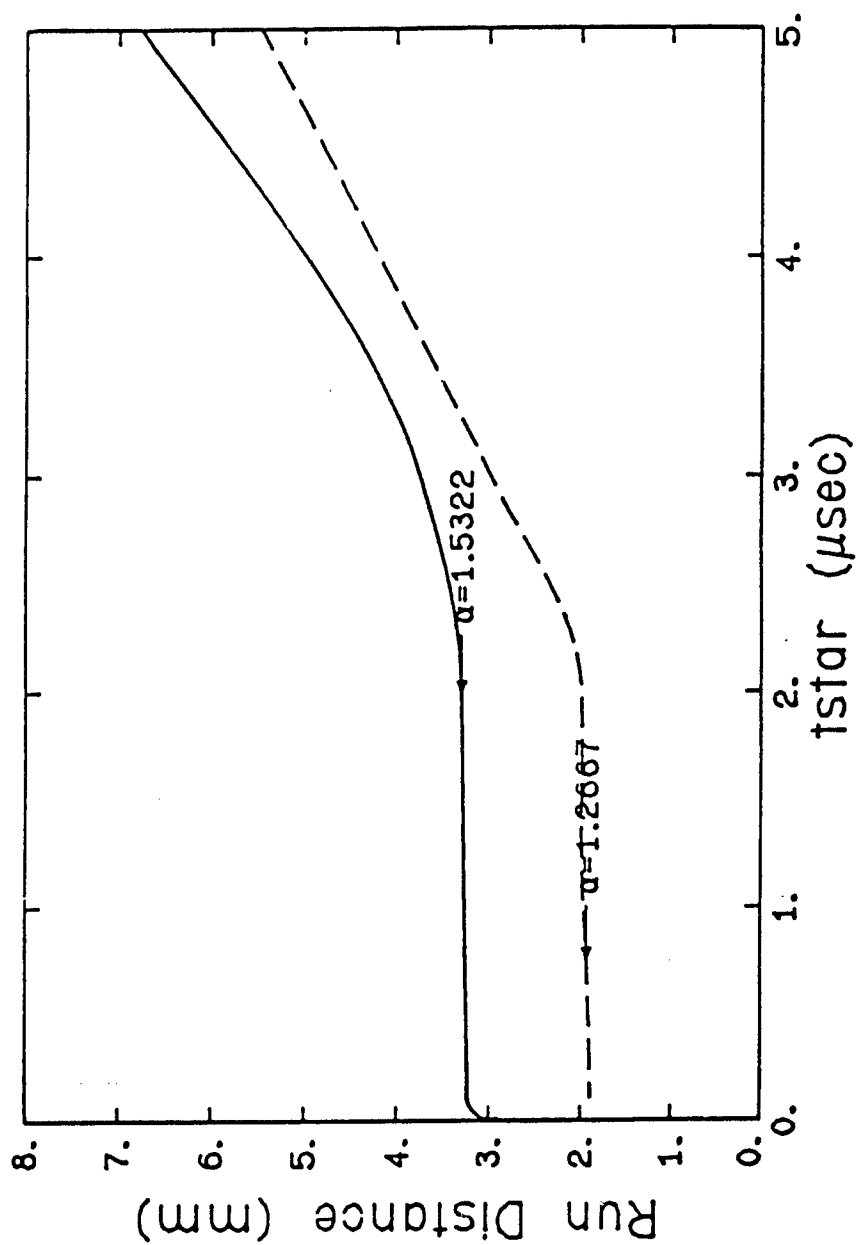
Figure 9   Predicted run-distance to detonation as a function of pressure rise time to reach 2.0 GPA. Two porosities are shown.

CHAPTER 2
COMPARISON WITH EXPERIMENTS

Introduction

Clearly there is a need to verify directly, or indirectly, the results which the model predicts. One must keep in mind that we predict the run-up to detonation (time and distance) for porous nitramine explosives (HMX, in particular) caused by rapid compression. As was defined in the previous chapter, by "rapid compression" we mean rise rates to peak pressures of the order of 1 GPa within times of many microseconds.

The variables affecting the run-up conditions which are most important (besides material properties) are:

(a) Porosity, ϕ_0; or $\alpha \equiv 1/(1-\phi_0)$; (typically $1.1 < \alpha < 1.5$)

(b) Peak pressure, P^*; (typically 0.1 to 10 GPa)

(c) Pressure rise time to P^*, defined as t^* (typically 1 to 10 μsec).

Review of the open literature which deals with the initiation to detonation of porous explosives indicates that although some data exists for the shock initiation ($t^* < 1$ μsec) of porous explosives, for our range of α and P^* there is no data for ramp compression processes, i.e. $t^* > 1$ μsec.

Nevertheless, we believe that the model should be tested against the existing shock initiation experiments. If the predictions match the observations, we will have increased confidence in the usefulness of the model. Conversely, if the data shows that the model insufficiently describes the run-up conditions, we will be further motivated to alter some of the assumptions and the subsequent analyses that go into it.

Shock Initiation Experiments [Porous Explosives]

Dick [13] performed shock initiation experiments using 75 mm diameter cylindrical samples of pour density (1.24 ± 0.04 g/cc, $\alpha = 1.5322$) HMX. In his experimental setup, the sample was attached to an aluminized PMMA driver plate, and a rotating-mirror camera was used to record the shock transit time through the explosive. Dick obtained his data points by utilizing a statistical analysis of large amounts of data to estimate mean material response.

It was possible to determine run distance and time to detonation for a given input stress through transit time measurements at a number of sample thicknesses.

Several calculations were made using an initial porosity ($\alpha = 1.532$) which matched the one used in experiments by Dick [13]. The results a.e shown in Fig. 10, a "Pop-plot" of P^* versus L_{SDT}. As the figure indicates, the slopes agree well for $P^* > 2.2$ GPa. For 1.3 GPa $< P^* < 2.2$ GPa, our calculations show little change in run-up distance as a function of P^*. As P^* drops below 1.3 GPa, L_{SDT} is predicted to rise sharply. In fact, our code failed to show a detonation occurring up to $t = 35$ μsec if $P^* < 1.1$ GPa. This pred'ction does not match Dick's data in this region, indicating that our model will need to be changed in order to match the "low" pressure initiation.

However, it goes without question that the model does a surprisingly excellent job in predicting the sensitivity of the run-to-detonation distance as a function of the shock pressure. No adjustments in any of the property constants or the kinetic rates for hot-spot decomposition were necessary.

From Fig. 10, one can fit a relation for both data and predictions. The data of Ref. [13] gives approximately that $L_{SDT} = 4.6/P^{0.56}$ while the model gives $L_{SDT} = 1.71/P^{0.49}$ if $P^* > 2$ GPA.

Lindstrom [14] examined the plane-wave shock initiation of a large particle size tetryl explosive at several pressing densities, ranging from essentially TMD ($\alpha \sim 1$) down to 75.1 percent TMD ($\alpha = 1.332$). Using the explosive wedge technique, the shock buildup to detonation was observed and recorded with a rotating mirror camera. From this film record, the run-distance and time to detonation were obtained.

Data was obtained for several initial shock strengths, which were dictated by the type of attenuator used. The inert attenuator consisted of either a single metal driver plate or two metal plates separated by a liquid. The driver plate free surface velocity was computed from charged-pin detector data and from this other shock parameters, such as initial shock strength, shock velocity, and particle velocity, were derived.

Figure 11 is the "Pop-plot" comparing results from our calculations to experimental results obtained by Lindstrom [14] for a porosity of $\alpha = 1.332$. Note that our calculations are representative of HMX whereas Lindstrom's data
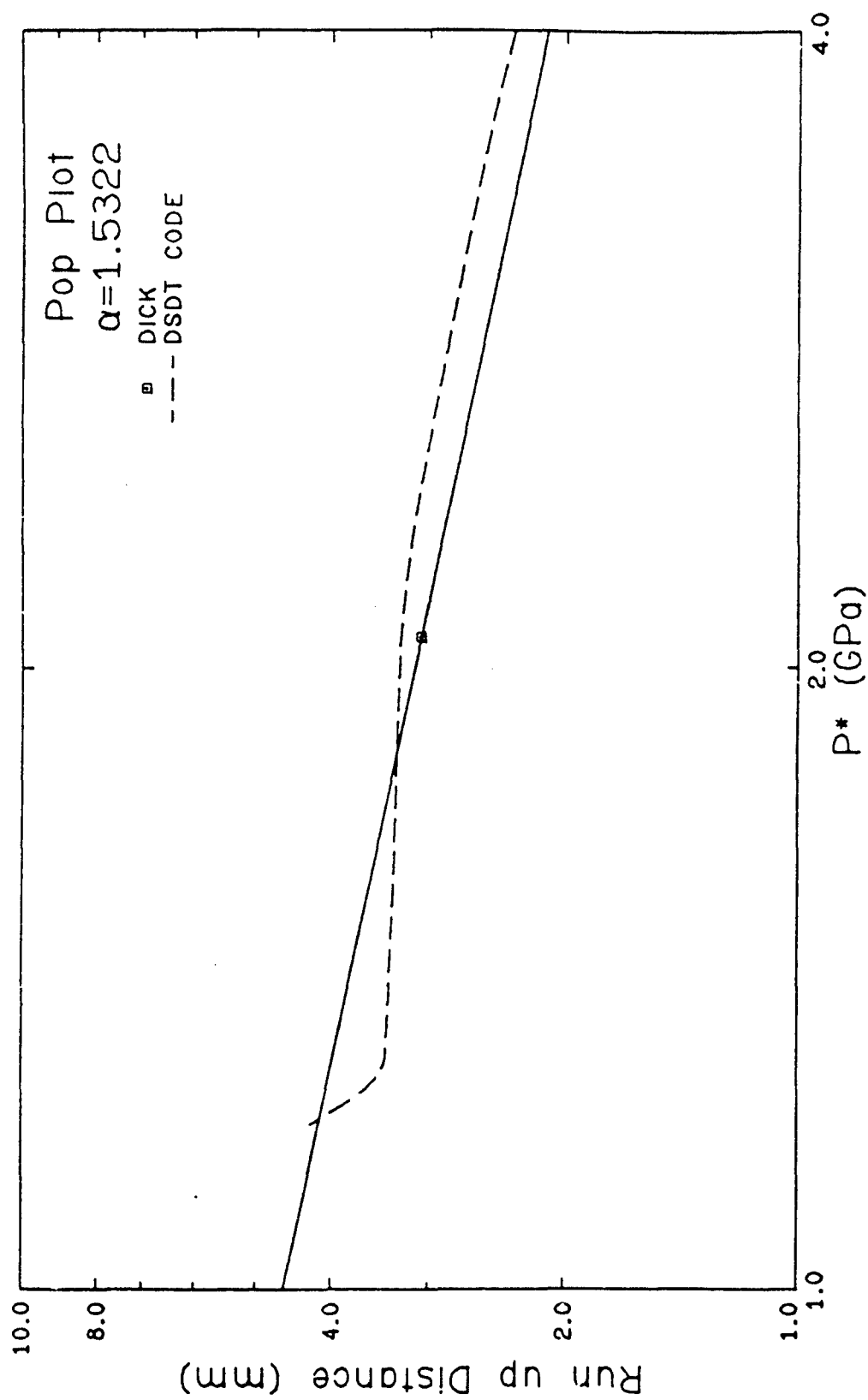
Figure 10 A closer view of the predictions shown in Figure 8 (run-distance vs. P*). Comparison of the data by J. J. Dick with predictions assuming t* = 1 μsec show good agreement.
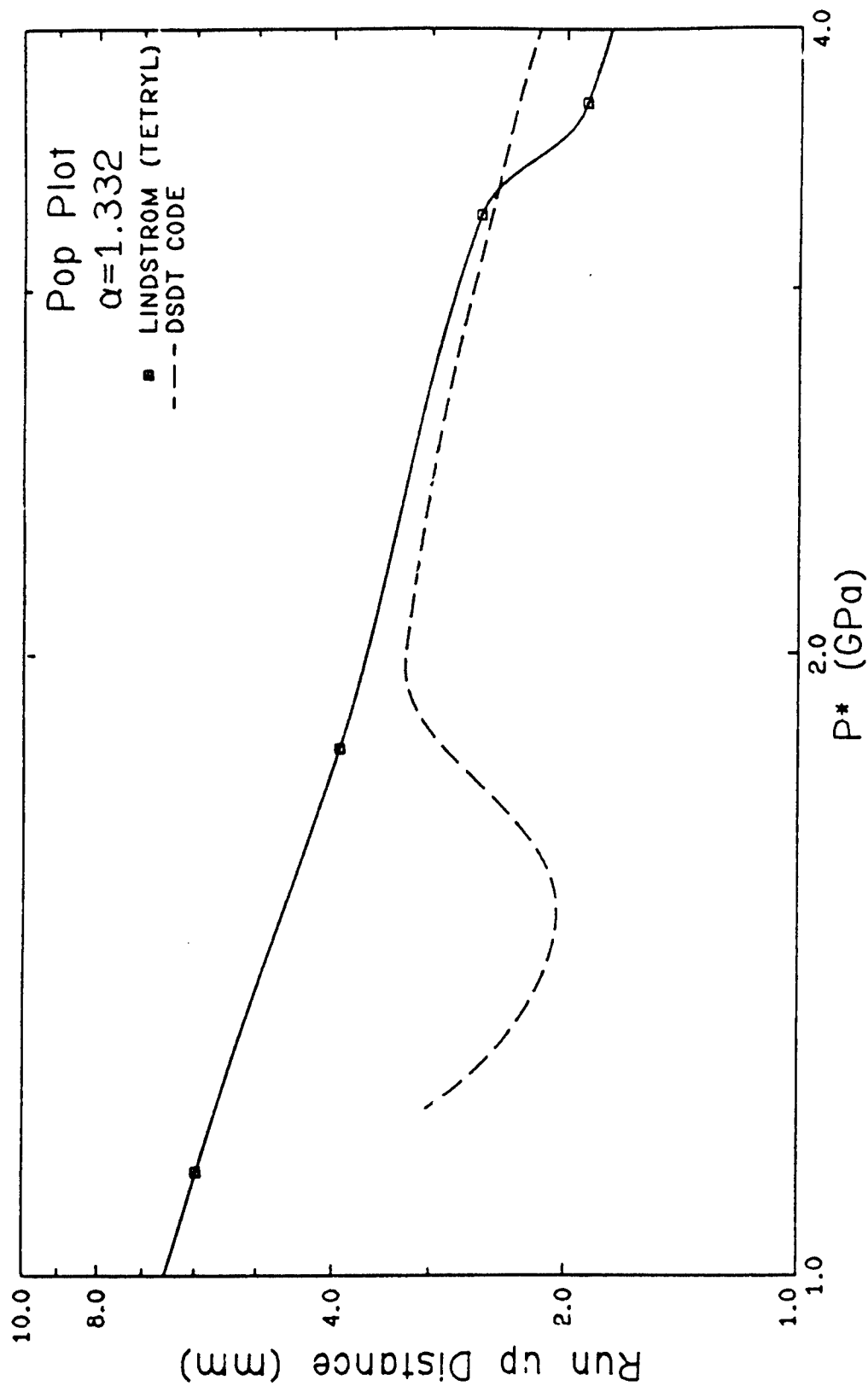
Figure 11 Run-distance to detonation vs. maximum input pressure for α = 1.332. The solid line represents data by I. E. Lindstrom for tetryl. The dash line represents predictions for HMX with the same porosity using a pressure rise time of t* = 1 μsec.

is for tetryl.   Nonetheless, the two are in very close agreement for
P* > 2 GPa. As P* drops below 2 GPa, however, our calculated run-up distances
exhibit unexpected behavior.   There is a minimum at P* = 1.5 GPa and below
this value our L_{SDT}'s rise sharply. The positive slope for 1.5 GPa < P* < 2
GPa may not be physically meaningful since increasing the shock strength
should not increase the run-up distance. Again, we will need to consider what
aspects of the shock initiation process at the relatively low pressures are
not being described by our model.

Sandusky and Bernecker [15] obtained shock initiation data for several
porous explosives, including class D HMX with a porosity of α = 1.37 and class
E HMX with a porosity of α = 2.27. In their experiments, the explosive was
radially confined and subjected to a long duration (>200 us), low-level shock
loading (<0.18 GPa).

The long duration loading was accomplished by using a powder gun to pro-
pel a 25.4 mm diameter by 305 mm long piston into the tube that contained the
porous bed.   It was generally found that when high confinement steel tubes
were used, the reaction grew rapidly and built to detonation. Often for these
experiments, the inner wall of the tube fragments showed the location of the
onset of detonation. In low confinement tubes, higher loadings were required
for a transition to detonation.

Typical run-up distances were large at these low initiation shock pres-
sures. For example, for HMX with α = 1.37, Sandusky and Bernecker reported
[15] the following:

Shock Pressure, P*	L_{SDT}
0.108 GPa	39 mm
0.1732 GPa	50 mm

An alternative to the run distance versus pressure plot, the so-called
"Pop-plot," in correlating shock initiation data is a log-log plot of run-up
distance versus the particle (material) velocity. Sandusky and Bernecker pre-
sented a composite plot of L_{SDT} versus u_p containing data for several differ-
ent explosives for a variety of porosities, including nearly voidless explo-
sives. They showed that almost all the data fit within a band of constant
slope. A straight-line fit to the data gives the relation $L_{SDT} = 1.6\ u_p^{-2.2}$

where L_{SDT} is in mm and u_p is in mm/µsec. The data covers particle velocities ranging from approximately 0.1 to 1.2 mm/µsec. This regime includes the very low shock initiation pressures such as those used by Sandusky. We believe this type of correlation is a slight improvement to that of the Pop-plot since a wider spectrum of data falls within a constant slope region. In particular, it permits the inclusion of data using low shock initiation pressures and data from nearly homogeneous explosives.

In Figs. 12 and 13, results from our calculations for α = 1.5322 are shown as a function of particle velocity behind the shock front. Figure 12 shows run-up distance to detonation, and Fig. 13 shows time to detonation. Here, u_p was calculated at the left boundary of the cast explosive, adjacent to the granulated bed. The solid line in each figure is an "eyeball" best fit of our calculations, which are shown by the solid circles. The results are qualitatively correct in that both run-up distance and time to detonation decrease linearly with increasing shock strength (represented by u_p). More quantitative data for this porosity (α = 1.5322) is needed in the future to enhance this parametric study.

Figures 14 and 15 repeat the L_{SDT} versus u_p plots for an initial porosity of α = 1.332. This porosity matches the one used by Lindstrom, whose data for porous tetryl is also included in these two figures. In each figure, the open circles are Lindstrom's data points and the solid line is an "eyeball" best fit of this data. The solid circles are results from our computer code. In Fig. 14, three of our calculations correlate well with the data. Two prediction points, well to the left of the data line, are results from runs using P*'s of 1.2 and 1.5 GPa. These points are from the troublesome region of Fig. 11, discussed earlier. The dashed line in Fig. 15 is an "eyeball" best fit of our calculations. Even though the slope was intended to match that of Lindstrom's data, our calculations still show good qualitative agreement. Notice that there are no "stray" points in the time to detonation plot as there were in the run-up distance to detonation plot in Fig. 14. In other words, as the initial peak input pressure was varied, the time to detonation did not exhibit the unexpected behavior that was found in the run-up distance to detonation.

All of the data obtained by Sandusky for porous HMX (as well as for other explosives) was for initiation by shocks of strengths less than 0.18 GPa,
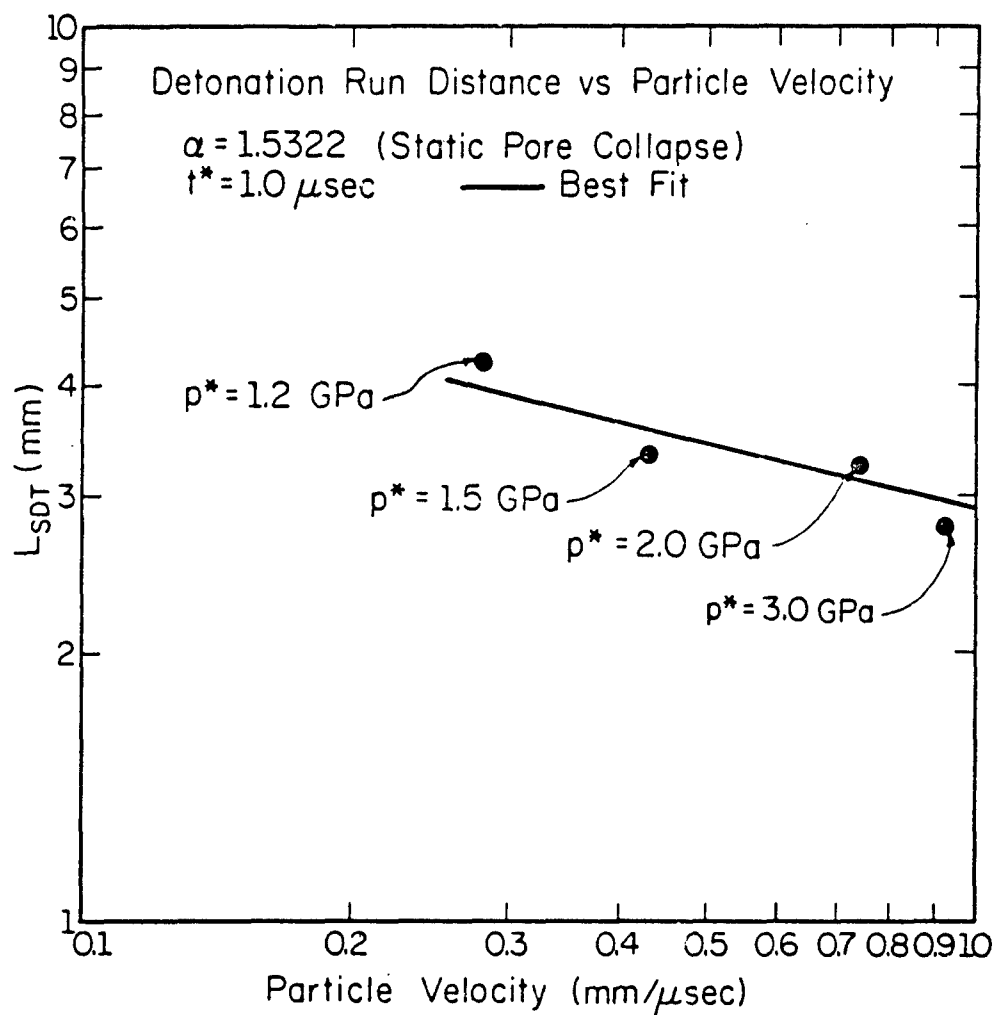
Figure 12 Predicted run-distance vs. imposed particle velocity at the
Zone 1/Zone 2 interface. (The peak input pressures needed to
provide the particle velocities are indicated in the figure.)

Figure 13 Predicted time to detonation vs. imposed particle velocity at the Zone 1/Zone 2 interface. (The peak input pressures needed to provide the particle velocities are indicated in the figure.)
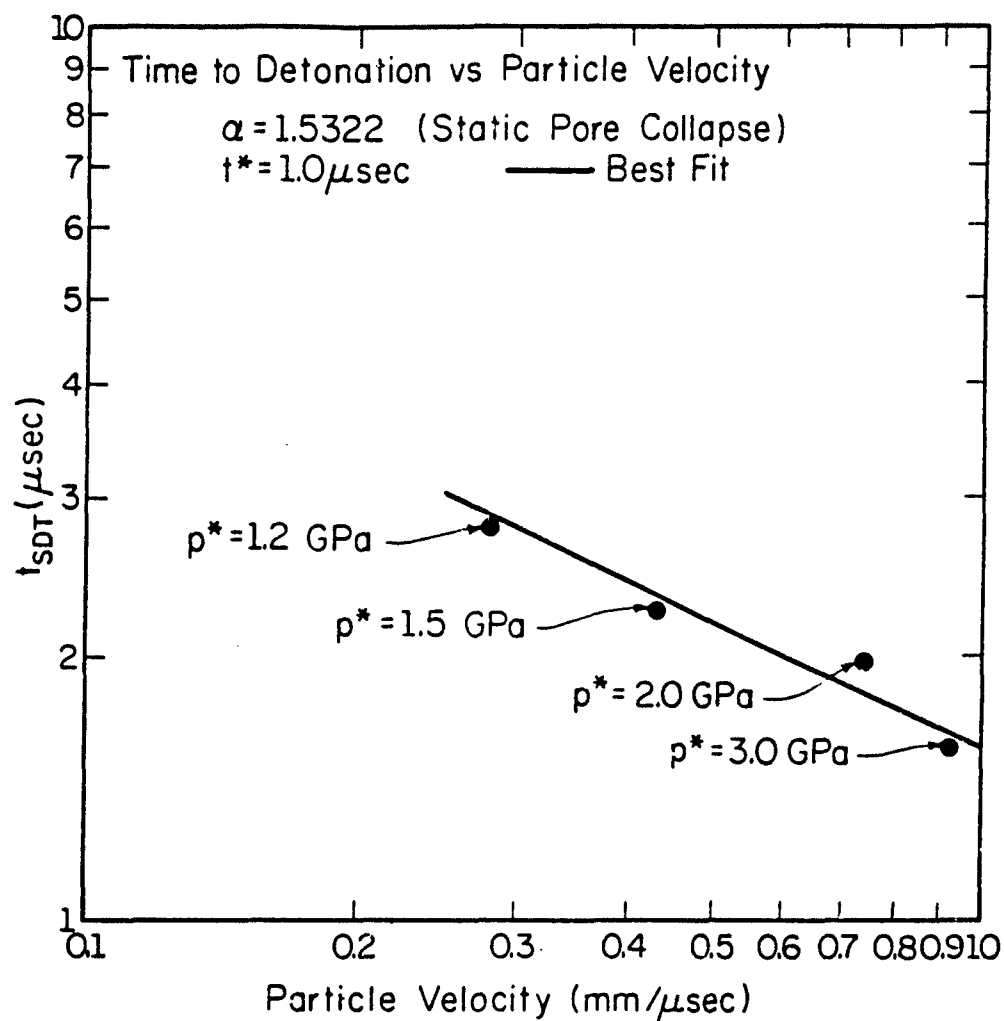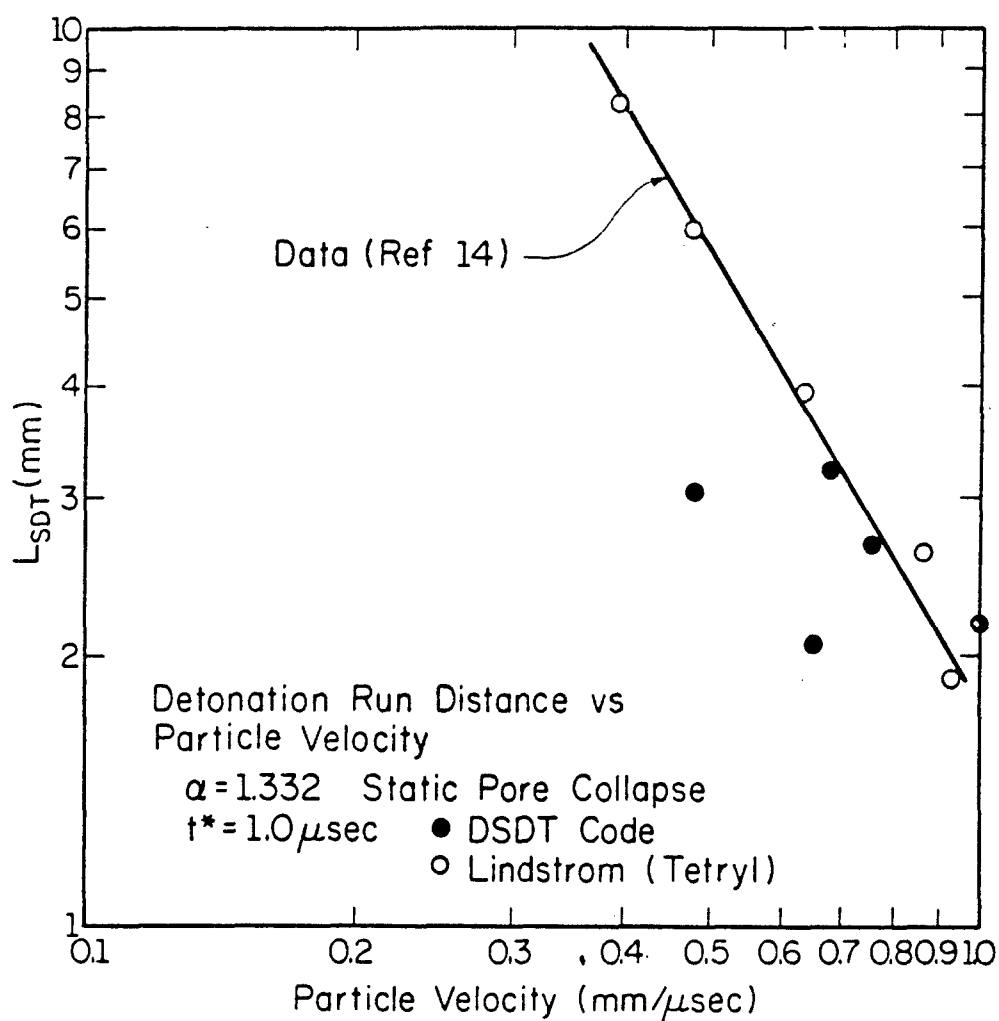
Figure 14 Predicted run-distance vs. particle velocity
compared with the data of I. E. Lindstrom.
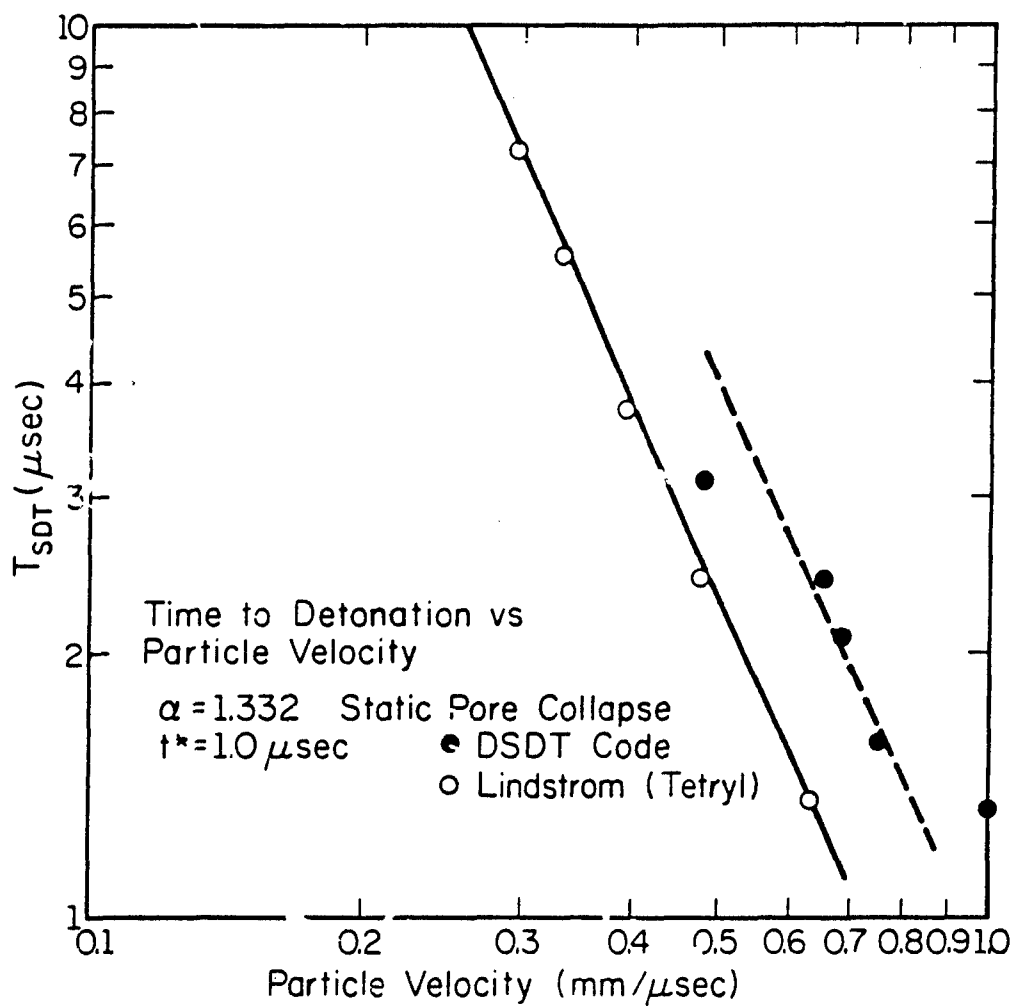
Figure 15 Predicted time to detonation vs. particle velocity
compared with the data of I. E. Lindstrom.

which resulted in very large run-up distances. In order for us to compare our calculations to this data, it is necessary to expand the time limits set on our computer runs. Even though this will likely be very expensive, limited runs of this nature will be done in the future. As previously pointed out, our model does not do as good a job in matching experiments as P*, the peak input pressure, drops below 2 GPa. By expanding the computer time and carrying out more low input pressure calculations, it is hoped that trends will be found that provide a clue to the shortcomings of the model in this region.

CHAPTER 3
MODEL EVALUATION: SENSITIVITY STUDIES
ON PORE COLLAPSE (AND OTHER COMPONENTS)

Arrhenius Kinetics

The first sensitivity study presented here is that of the "activation temperature" term which is found in Eq. (1.13). "Activation temperature" is the name given to the variable grouping $E^*/\bar{R}$, where E^* is the activation energy and $\bar{R}$ is the universal gas constant. Physically, as used in the Arrhenius burn model of Eq. (1.13), the activation energy represents the minimum value of molecular energy needed to guarantee chemical reaction. Figure 16 is a plot of run-up distance to detonation as a function of activation temperature, or ACTEMP, for two different values of initial porosity. Here, ACTEMP is normalized with respect to the "standard" ACTEMP of 14400 K, which is the value used for all other calculations presented in this report. A ramp wave input with a peak pressure of 2 GPa and a rise time of 10 µsec was used for these runs, as well as the static pore collapse model (to be discussed in the next section) and a finite difference grid spacing of $\Delta x = 0.5$ mm.

Upon examining the figure, both curves initially show steep increases in L_{SDT} as ACTEMP increases. Intuitively, this is expected since raising the activation energy means more energy is required to initiate reaction. More time is needed for the coalescing stress waves to build up to the required energy level. During this time the stress front continues to propagate through the explosive. Thus, reaction is finally initiated further downstream. Surprisingly, the similarities between the two curves end after their initial ascents. The solid curve, for $\alpha = 1.1176$, levels out only temporarily before sharply rising again, showing no further indication of reaching a steady value. On the other hand, the dashed curve, for $\alpha = 1.2667$, reaches a peak before dropping slightly to a constant value. Further investigation is needed to clarify why the more porous sample is not affected by changes in ACTEMP in this constant region. Clearly other mechanisms are involved.
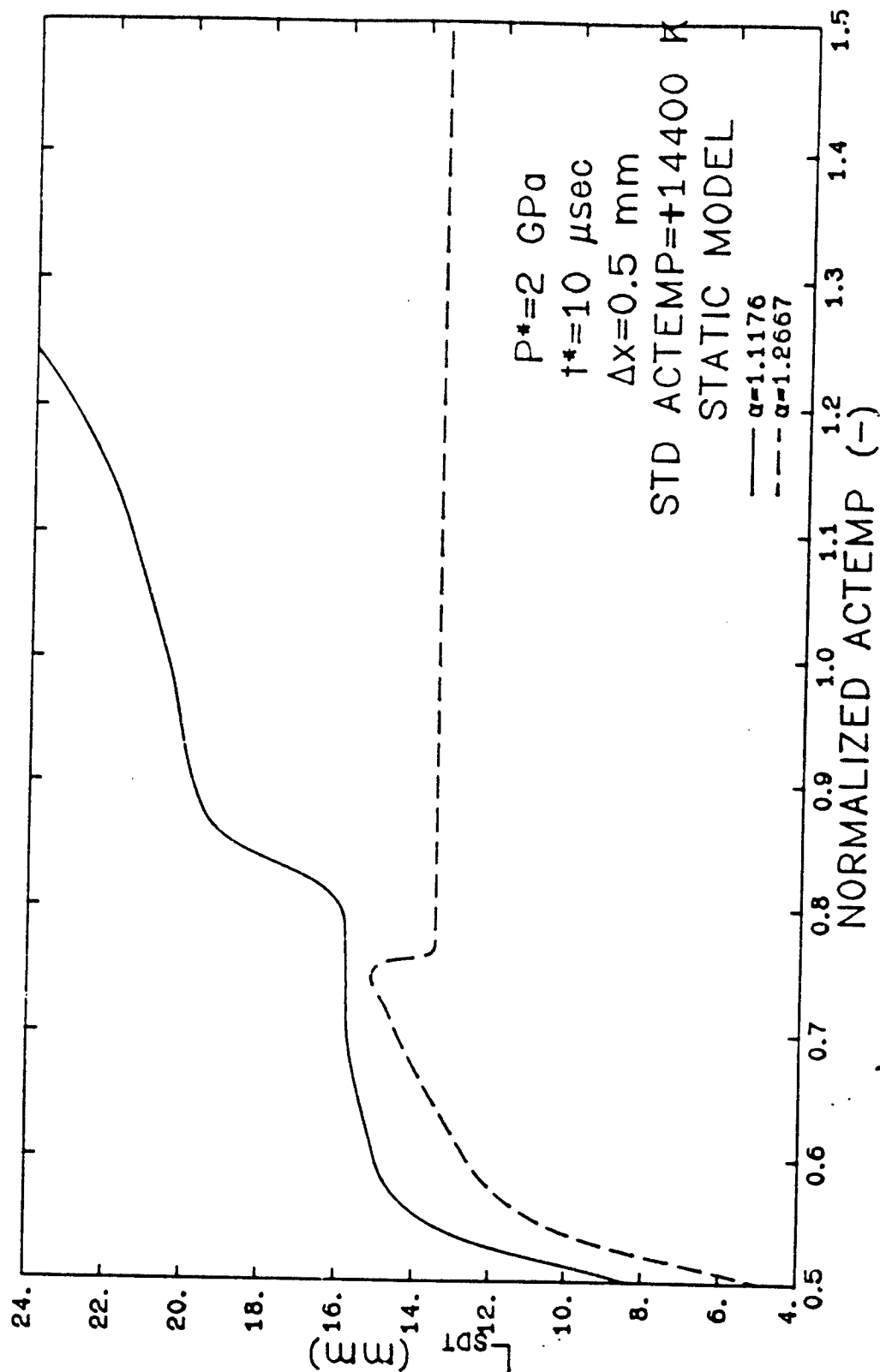
Figure 16 Predicted run-distance to detonation as a function
of the activation energy for explosive decomposition.
Two different initial porosities are studied.

Pore Collapse Model: Static Compaction Assumption

As mentioned in Chapter 1, the pore collapse process is represented by a three step static compaction model. A detailed derivation of this model is given by Carroll and Holt in Ref. [8]. A brief description is presented here. The static model involves no rate dependence term in describing the pore collapse process. The relation used is

$$P = P_{eq}(\alpha) \tag{3.1}$$

where P is the applied pressure and P_{eq} is the equilibrium pressure of the solid corresponding to the instantaneous porosity. For instantaneous material response (an assumption inherent with the use of the static model), P is also equal to the pressure of the aggregate porous material, which is a volume average of the pressure of the solid material calculated from an appropriate constitutive relation and the pressure of the gas inside the pore (assumed to be at atmospheric pressure).

Carroll and Holt [8] define three regimes of compression: the elastic, elastic-plastic, and the plastic phases. The equilibrium pressure for each phase and the appropriate range over which each applies are given by

elastic phase $\alpha_0 \geq \alpha \geq \alpha_1$

$$P_{eq}(\alpha) = \frac{4G(\alpha_0 - \alpha)}{3\alpha(\alpha - 1)} \tag{3.2}$$

elastic-plastic phase $\alpha_1 \geq \alpha \geq \alpha_2$

$$P_{eq}(\alpha) = \frac{2}{3} Y \left\{ 1 - \frac{2G}{Y\alpha}(\alpha_0 - \alpha) + \ln \left[\frac{2G(\alpha_0 - \alpha)}{Y(\alpha - 1)} \right] \right\} \tag{3.3}$$

plastic phase $\alpha_2 \geq \alpha > 1$

$$P_{eq}(\alpha) = \frac{2}{3} Y \ln\left(\frac{\alpha}{\alpha - 1}\right) \tag{3.4}$$

where the limits between the phases are expressed as

$$\alpha_1 = \frac{2G\alpha_0 + Y}{2G + Y} \quad \text{and} \quad \alpha_2 = \frac{2G\alpha_0}{2G + Y}. \tag{3.5, 3.6}$$

To calculate the porosity at each timestep in the computer program, an iterative process is used to solve Eq. (1) utilizing the appropriate relation for P_{eq}. The individual terms in the above equations are defined in Table 2.

Pore Collapse Model: Dynamic Compaction Assumption

Recently the static pore collapse model was replaced by two different versions of dynamic material response models. The first version discussed here was derived by Carroll and Holt [8], whose corresponding static model was used previously in our code. In fact, their static model is a direct result of their dynamic model upon the assumption that the applied pressure rate is infinitesimally small. In this section, Carroll and Holt's dynamic model will be investigated extensively, including many comparisons and references to the static model. Following this, a brief look at a second dynamic model, that of Kooker and Anderson [16], will be made.

Dynamic Model Version 1: Carroll and Holt [8]

A detailed derivation of this model is given in Ref. [8]. A brief description is presented here. The dynamic relation is given by

$$\tau^2 \, Y \, Q(\ddot{\alpha}, \dot{\alpha}, \alpha) = P - P_{eq}(\alpha). \tag{3.7}$$

The strong rate dependence of the pore collapse process is embedded in the term $Q(\ddot{\alpha}, \dot{\alpha}, \alpha)$, which is given by

$$Q(\ddot{\alpha}, \dot{\alpha}, \alpha) = - \ddot{\alpha}[(\alpha-1)^{-1/3} - \alpha^{-1/3}] + \frac{1}{6} \dot{\alpha}^2 [(\alpha-1)^{-4/3} - \alpha^{-4/3}] \tag{3.8}$$

The term τ in Eq. (3.7) is a material time constant (having the physical dimension of time) defined by

$$\tau^2 = \frac{\rho \, a_0^2}{3Y(\alpha_0-1)^{2/3}}. \tag{3.9}$$

The terms in this equation are defined in Table 2.

P and P_{eq} are as defined for the static model. Note that P is actually the applied pressure which, because of the finite material response times as-

Table 2 Nomenclature

Symbol	Definition	Units	Typical Value
α_o	initial porosity	-------	1.1176
α	instantaneous porosity	--------	$\alpha_o \geq \alpha \geq 1$
Y	yield strength	MPa	51.7 (HMX)
G	shear modulus	MPa	3516 (HMX)

ADDITIONAL TERMS USED IN DYNAMIC MODEL

ρ	initial density of the solid	g/cc	1.90 (HMX)
a_o	initial pore radius	μm	20
Δ	time increment	nsec	5

sociated with the dynamic model, is not equal to the pressure of the aggregate material, except possibly for very small applied pressure rates. Since the applied pressure is only known at one location (and thus for only one finite difference cell), the material boundary, we are forced to treat this term just as was done for the static model. That is, P is assumed to be equal to the pressure of the aggregate material.

Upon examining Eq. (3.6), it is evident that if the ratio of yield strength to shear modulus is small, which is generally the case (for HMX, $Y/G = 0.0147$), the change in porosity during the elastic and elastic-plastic phases is small. Thus, to simplify the analysis of Eq. (3.7) a good approximation may be made by neglecting rate dependence during these first two phases. In doing so, Eq. (3.7) can be rewritten by substituting Eq. (3.4) for $P_{eq}(\alpha)$,

$$\dot{r}^2 \, Y \, Q(\alpha, \dot{\alpha}, \alpha) = P - \frac{2}{3} \, Y \, \ln \left(\frac{\alpha}{\alpha - 1} \right).$$
(3.10)

Carroll and Holt [8] used the following finite difference form of Eq. (3.10) for numerical analysis.

$$\alpha_{N+1} = 2\alpha_N - \alpha_{N-1} + [1/f_1(\alpha_N)] \left[\frac{1}{6} (\alpha_N - \alpha_{N-1})^2 \, f_4(\alpha_N) \right.$$

$$\left. - (\Delta^2 / r^2 Y) \{ P_N - \frac{2}{3} \, Y \, \ln [\frac{\alpha_N}{\alpha_N - 1}] \} \right]$$
(3.11)

where $f_s(\alpha) = (\alpha-1)^{-s/3} - \alpha^{-s/3}$.

In summary, the dynamic model consists first of modeling statically the elastic and elastic-plastic phases of compaction, where the change in porosity is very small. When the transition porosity α_2 is attained, Eq. (3.11) is used to calculate new values of porosity. The initial conditions needed for Eq. (3.11), which are α_N and α_{N-1}, are those values calculated from the previous two timesteps. Note that this form of the dynamic model gives an explicit expression for α. No iteration is required.

The first comparison between the static and dynamic models will be that of run-up distance to detonation (L_{SDT}) as a function of initial porosity. The results are plotted in Fig. 17. For these runs, an input ramp wave with a

peak pressure of 2 GPa and a rise time of 10 μsec was used, along with a finite difference grid spacing of 0.5 mm. Runs using the dynamic model also required the initial pore radius (a_0) to be input. Here, 20 μm was used.

Upon examining Fig. 17, the two models predict the same general trend over the whole range of porosities. The curves initially show rapid declines in L_{SDT} since the more porous materials have a higher hot spot volume, and thus more irreversible energy is deposited to initiate reaction. If the two curves were extended to include lower porosities, each would approach an asymptote at around $a = 1.02$. This means that for porosities at or below this value, detonation ceases to occur in our 10 cm bed for the given ramp input. However, for $a \geq 1.35$, the L_{SDT}'s start to rise. In this range of higher porosities, even though the hot spot volumes are greater, the local density of the material has decreased to a point where its effect overrides that of hot spot volume. As previously concluded for the static pore collapse runs, the higher porosity material (i.e. the material with the lower local density) has less mass and thus less energy upon decomposition available to support a shock front. Thus the distance at which a steady state detonation is reached is increased. Although just a conjecture here, the higher porosity material is more likely to bend and distort the shock. This possibility could be studied if the present analysis were extended to two dimensions.

Another factor to discuss is the equivalent volume concept inherent in the hot spot model used here; that is, the initial volume of hot spot material is equal to the original pore volume. This assumption is reasonable for, and intended for, low porosities. This fact should be kept in mind when considering higher porosities where the concept may not be accurate. A revision of the equivalent volume concept for high porosities ($a > 1.25$), which is a topic of current investigation, might significantly affect the results.

Referring back to Fig. 17, for $a \geq 1.19$, the dynamic model predicts L_{SDT}'s that are at or below those predicted by the static model while the reverse is true for $a \leq 1.19$. In addition, the L_{SDT}'s from the dynamic model are less sensitive to changes in porosity in the range $1.25 \leq a \leq 1.53$. The static curve has a well defined minimum at $a = 1.36$ whereas the dynamic curve has a less apparent minimum at $a = 1.33$.

Table 3 compares L_{SDT} and t_{SDT} (time to detonation) values from the static and dynamic models for a shock wave input ($t^* = 1$ μsec) as well as for
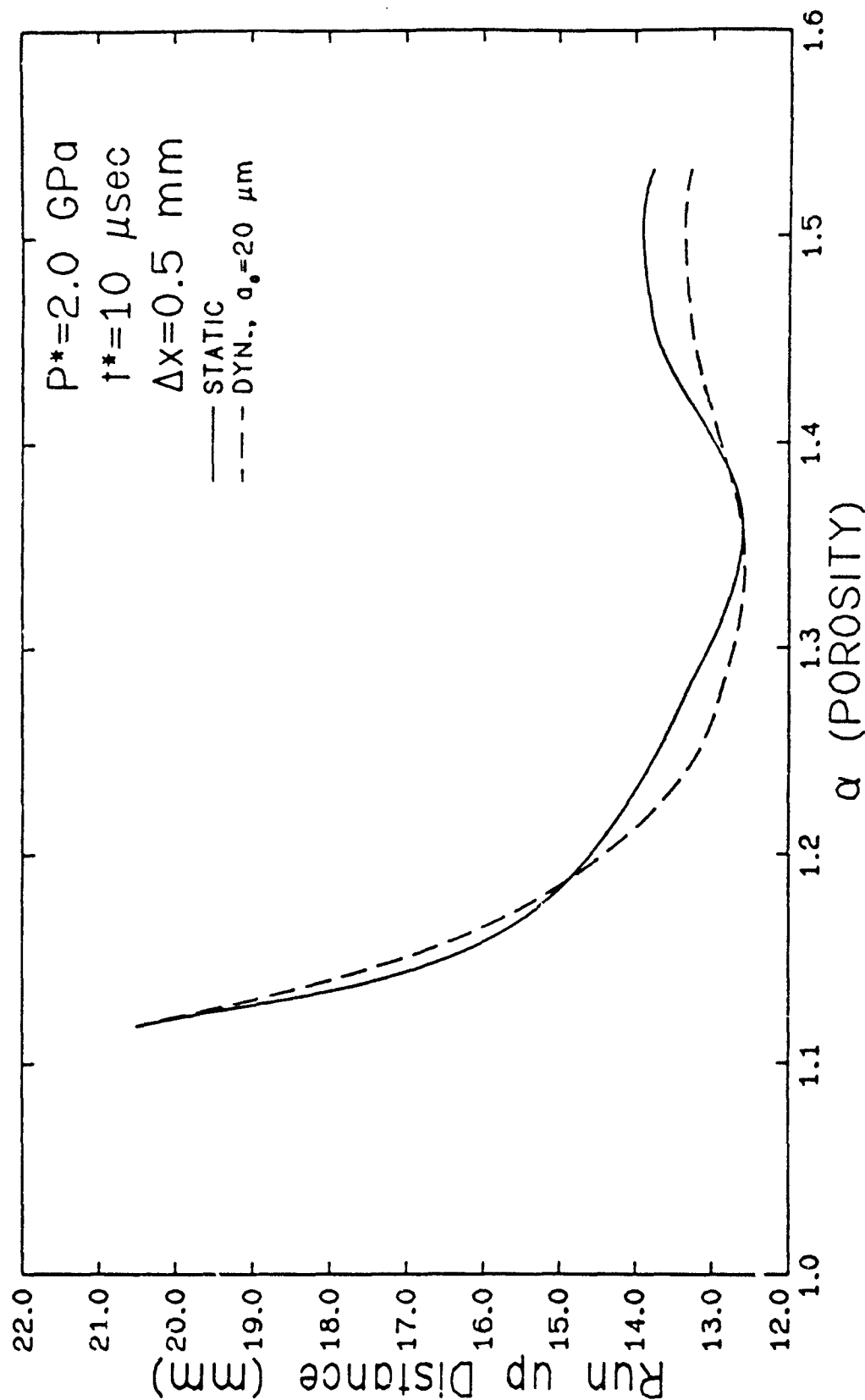
Figure 17 Predicted run-distance to detonation vs. porosity comparing the static pore collapse assumption to the dynamic pore collapse model of Carroll and Holt.

Table 3 Comparison of Run Up Distance and Time to Detonation
$\alpha = 1.2667$, $P* = 2$, $t^* = 1, 10$

	ramp L_{SDT} (mm)	shock
	$t^* = 10$ μsec	$t^* = 1$ μsec
Static	13.4728	1.972
Dynamic ($a_0 = 20$ μm)	12.9756	1.9495
% Diff (of dynamic)	-3.7%	-1.1%

	t_{SDT} (μsec)	
	$t^* = 10$ μsec	$t^* = 1$ μsec
Static	11.23	2.095
Dynamic ($a_0 = 20$ μm)	10.99	2.05
% Diff (of dynamic)	-2.1%	-2.1%

the ramp wave input just discussed. The porosity considered here is α = 1.2667. This comparison is done to show that the dynamic compaction model gives consistent results (compared to the static model) for input rise times approaching a true shock. The consistency of the static model for these inputs has already been demonstrated.

The variation of L_{SDT} with peak pressure input for both compaction models is shown in the "Pop plot" in Fig. 18 for α = 1.5322. The solid line on the plot is experimental data obtained by Dick [13] for this same porosity. The results clearly indicate almost no deviation between the static and dynamic models for the shock input (t* = 1 μsec) and only a slight deviation when P* < 2.5 GPa for the ramp input (t* = 10 μsec).

The next parametric study examines the effect of initial pore radius on L_{SDT} for the dynamic compaction model. Figure 19 is a plot of L_{SDT} versus a_0 for four different porosities using a ramp input of P* = 2 GPa and t* = 10 μsec. For a_0 < 40 μm, the run up length in each porous sample is virtually independent of a_0. However at a_0 = 40 μm, L_{SDT} in the α = 1.2667 sample drastically drops. This is assumed to be a "trouble spot" with this dynamic model. For a_0 > 40 μm, the α = 1.2667 and α = 1.1875 curves oscillate as a_0 increases, which also can be attributed to numerical difficulties.

Further evidence of numerical difficulties with the dynamic model is shown in Fig. 20, which shows the hot spot temperature profile about 2.5 μsec after detonation for a grid spacing of 0.5 mm, a porosity of 1.1176, a pore radius of 39 μm, and a ramp input of P* = 2 GPa and t* = 10 μsec. The profile is marked by sharp oscillations, which are a result of the explicit finite difference relationship used to calculate the porosity at each timestep.

Figure 21 is a hot spot temperature profile using the static compaction model with all inputs being the same as those for Fig. 20. Here the oscillations are very small, almost negligible, indicating a greater stability of the static model. Note also that the average hot spot temperature is about 800 K greater using the dynamic model.

Next, the effect of grid size and the length of the timestep on L_{SDT} are examined. The finite difference cell size used by Krier and Cudak [1] and previously in this research was 0.5 mm. However, reducing the cell size to 0.25 mm caused L_{SDT} to go up by about 10 percent regardless of whether the static or dynamic model was used. Run up lengths from the static model were
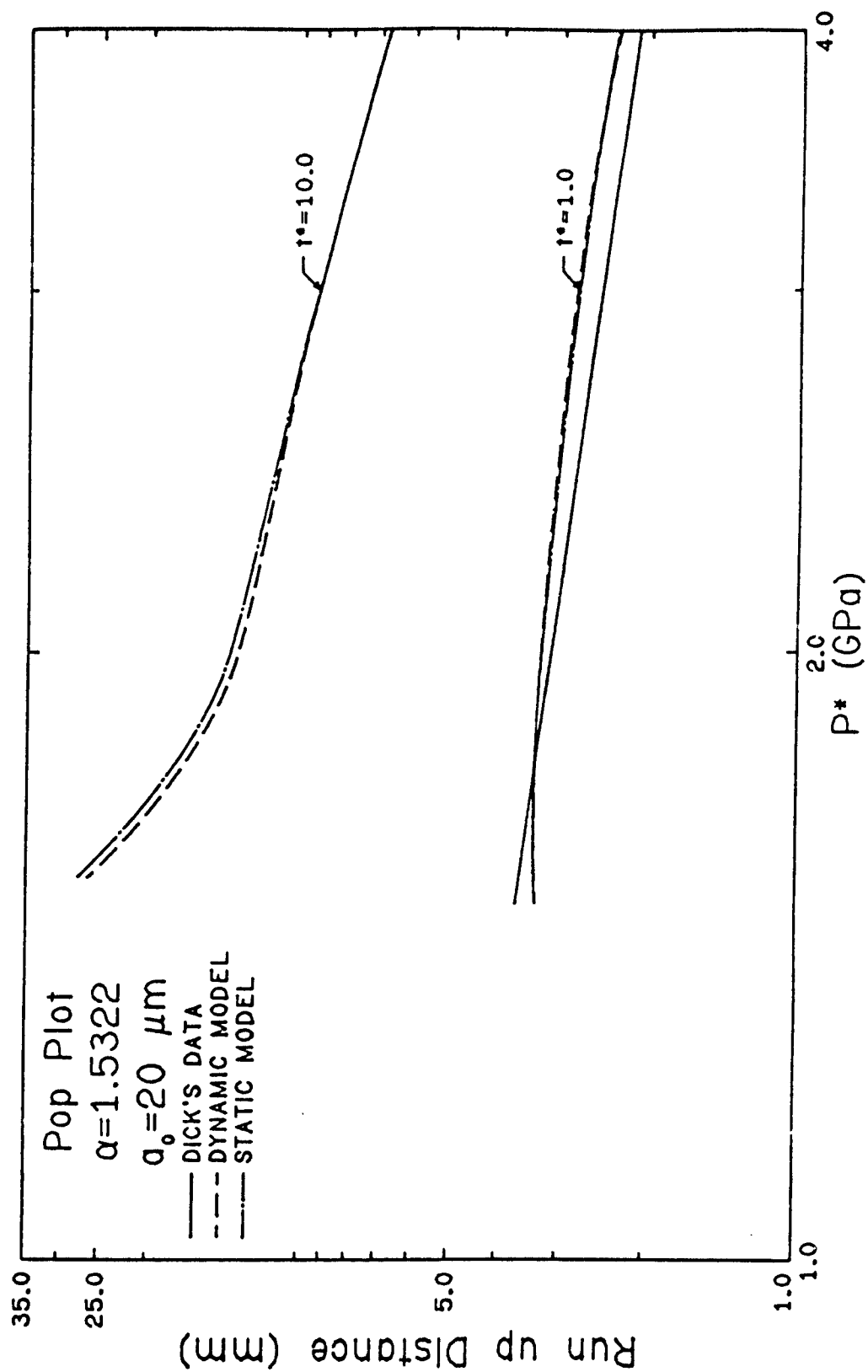
Figure 18   Run-distance to detonation vs. peak input pressure comparing data by J. J. Dick with predictions for both dynamic and static pore collapse.
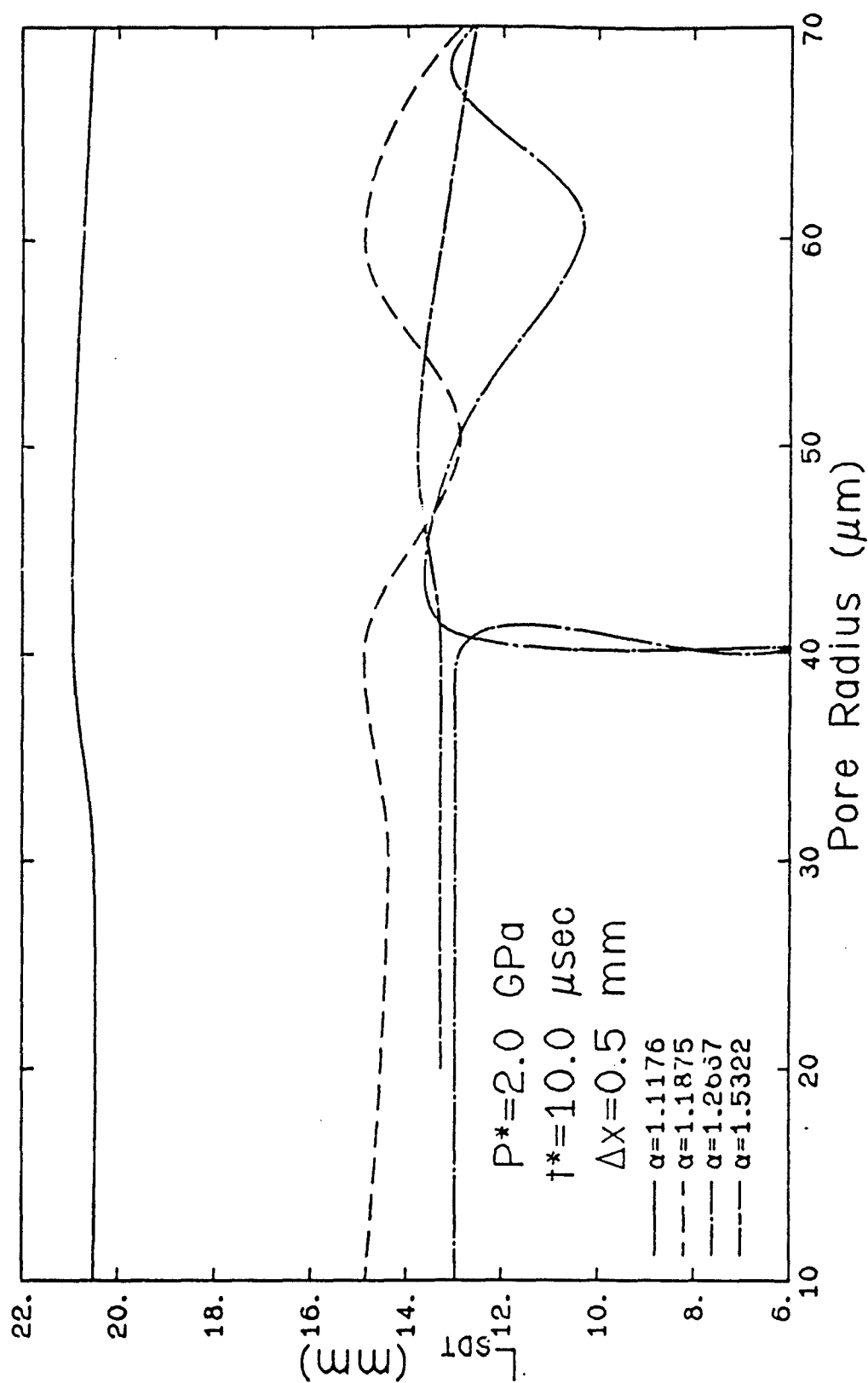
Figure 19 Predicted run-distance to detonation vs. initial pore radius for four different porosities using Carroll and Holt's dynamic pore collapse model. For the imposed P* and t* one observes a complex behavior.
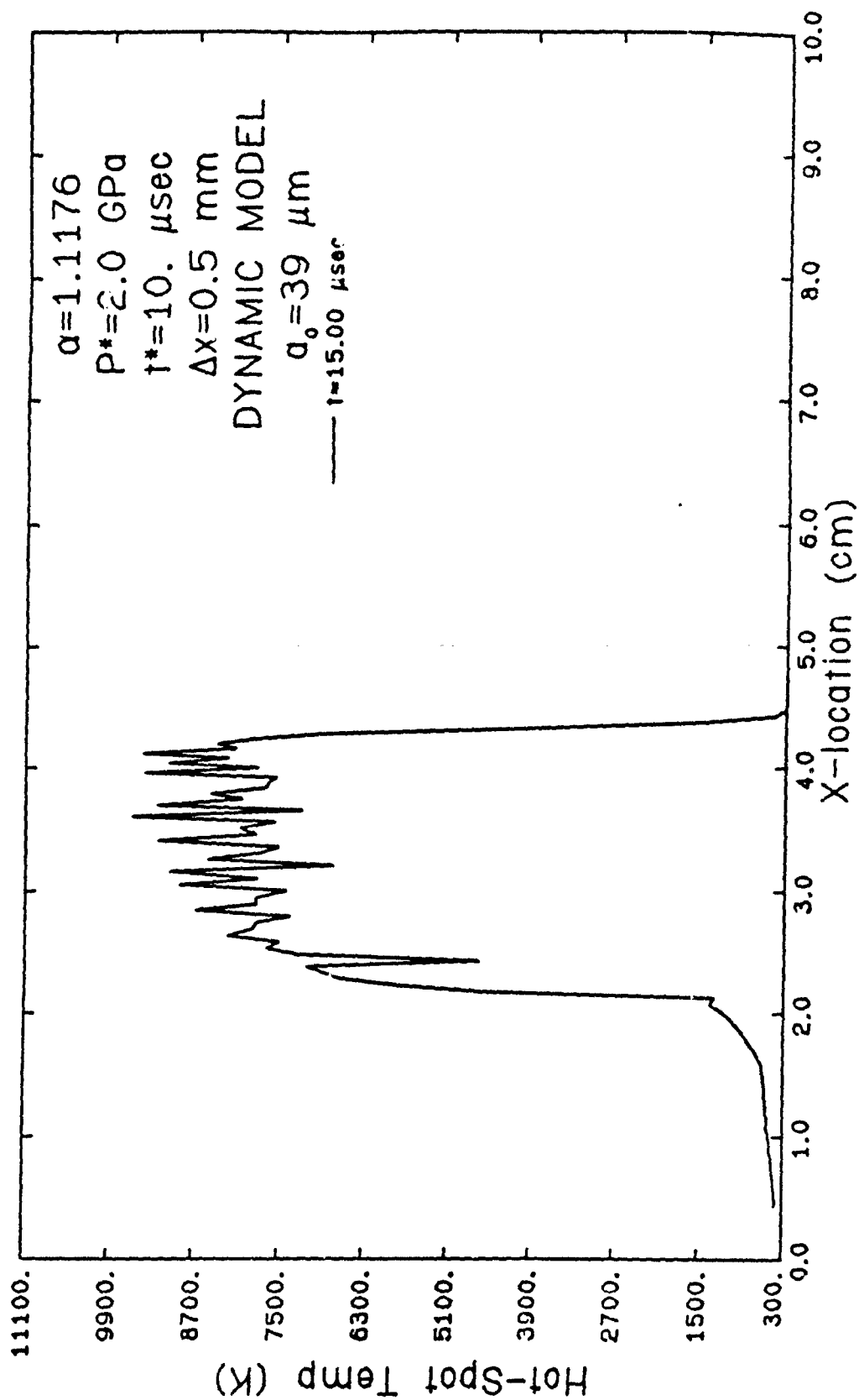
Figure 20 Hot spot temperature profile in the explosive bed about 2.5 μsec after detonation. The sharp oscillations are due to numerical difficulties with the use of Carroll and Holt's dynamic pore collapse model.
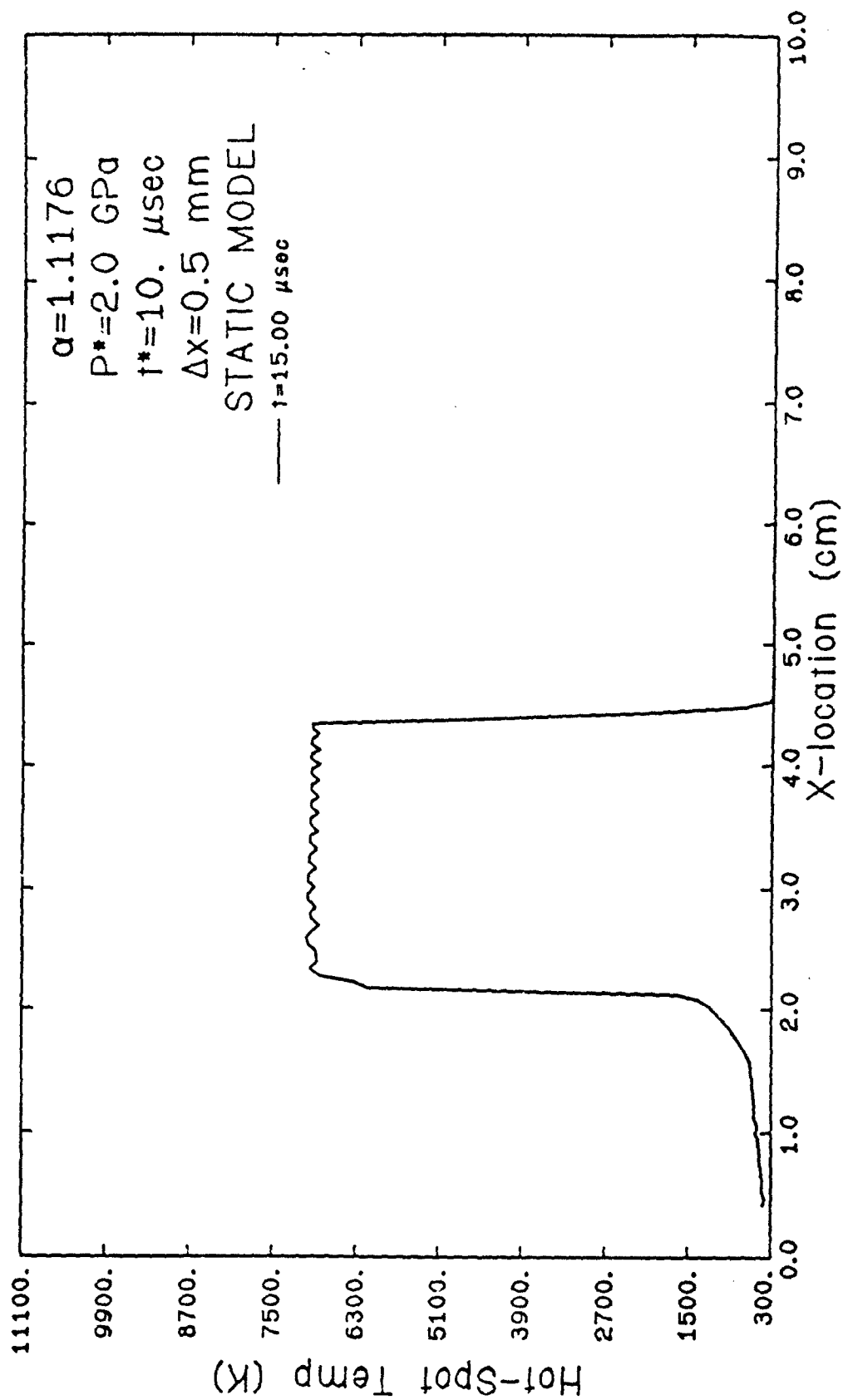
Figure 21 Hot spot temperature profile in the explosive bed about 2.5 μsec after detonation using the static pore collapse model.

virtually insensitive to further reductions in cell size down to $\Delta x = 0.125$ mm. On the other hand, run up lengths from the dynamic model dropped by more than 63 percent when 0.167 mm $\leq \Delta x \leq 0.20$ mm! These results are summarized in Table 4.

Figures 22 and 23 present hot spot temperature profiles for runs identical to those from Figs. 20 and 21, respectively, except that Δx has been reduced from 0.5 mm to 0.25 mm. (The profiles are narrower in Figs. 22 and 23 because detonation occurred later for $\Delta x = 0.25$ mm.) Comparing the two static runs, the oscillations in Fig. 23 are sharper, yet they remain very small and stable. Also, the values of the hot spot temperatures for the two runs are only slightly different. Comparing the two dynamic runs, the oscillations in Fig. 22 remain large, as they were in Fig. 20. Furthermore, the reduction in Δx caused an increase in the average hot spot temperature by more than 2000 K!

The timestep used in all previous runs using the static model was 5 nsec. Extending this analysis to include timesteps ranging from 4 nsec to 10 nsec gives run up lengths that do not vary significantly. However, the dynamic model gives L_{SDT}'s varying by up to 11 percent in the range of 4 nsec $\leq \Delta t \leq 10$ nsec. These results are summarized in Table 5.

It was initially conjectured that the numerical difficulties with the dynamic model could be due to an incorrect artificial viscosity, a term which is included in the momentum equation to account for irreversibilities across the shock wave. However, the sharp oscillations in the hot spot temperature remained for all values of artificial viscosity tried. Figure 24 is a plot of L_{SDT} versus ARV, the coefficient of quadratic artificial viscosity. The value of ARV used in all runs up until now was 3.0. Included here are the static results as well as dynamic results for pore radii of 39 μm and 50 μm. Other inputs were $\alpha = 1.1176$, $P^* = 2$ GPa, $t^* = 10$ μsec, and $\Delta x = 0.25$ mm. The static results given by the solid line show a small, smooth increase in L_{SDT} as ARV increases. The dynamic results, however, once again exhibit very erratic behavior. There seem to be no similarities between the two dynamic curves representing the two pore radii. Recall that Fig. 19, where $\Delta x = 0.50$ mm, showed no dependence of L_{SDT} on pore radius for $\alpha = 1.1176$, $P^* = 2$ GPa, $t^* = 10$ μsec. Note also the "trouble spot" at ARV = 2.0 for $a_0 = 39$ μm. To further announce the instability of the dynamic method, this

Table 4 Effect of Finite Difference Cell Size on Computed Results Using
(a) The Dynamic Model and (b) The Static Model (P* = 2 GPa, t*
= 10 usec, α = 1.1176, a_0 = 39 um, Δt = 5 nsec)

Run	Δx (mm)	L_{SDT} (mm)	Deviation of L_{SDT} from Run 1	t_{SDT} (usec)
1	0.50	20.9486	-----	12.45
2	0.25	23.0206	+ 10%	13.22
3	0.20	7.5382	- 64%	8.17
4	0.167	7.6951	- 63%	6.26

(a)

Run	Δx (mm)	L_{SDT} (mm)	Deviation of L_{SDT} from Run 1	t_{SDT} (usec)
1	0.50	20.5049	----	12.41
2	0.25	22.5351	+ 10%	13.13
3	0.20	22.8153	+ 11%	13.155
4	0.167	23.0246	+ 12%	13.235
5	0.125	23.1690	+ 13%	13.280

(b)

Figure 22 Hot spot temperature profile in the explosive bed about 1.8 μsec after detonation using the reduced finite difference cell size of Δx = 0.25. All other input data are identical to those of Figure 20. The sharp oscillations do not disappear for the given cell size reduction.
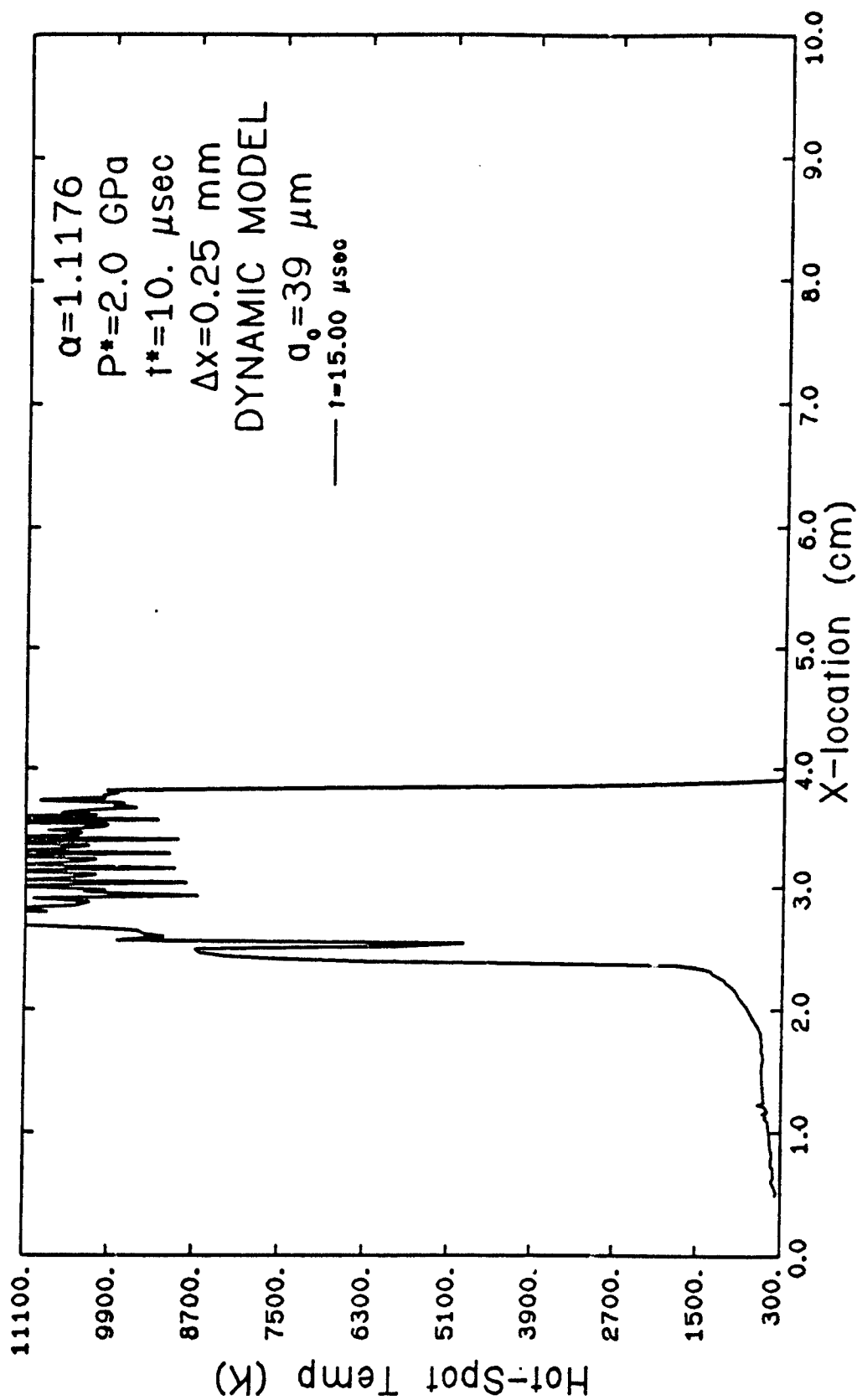
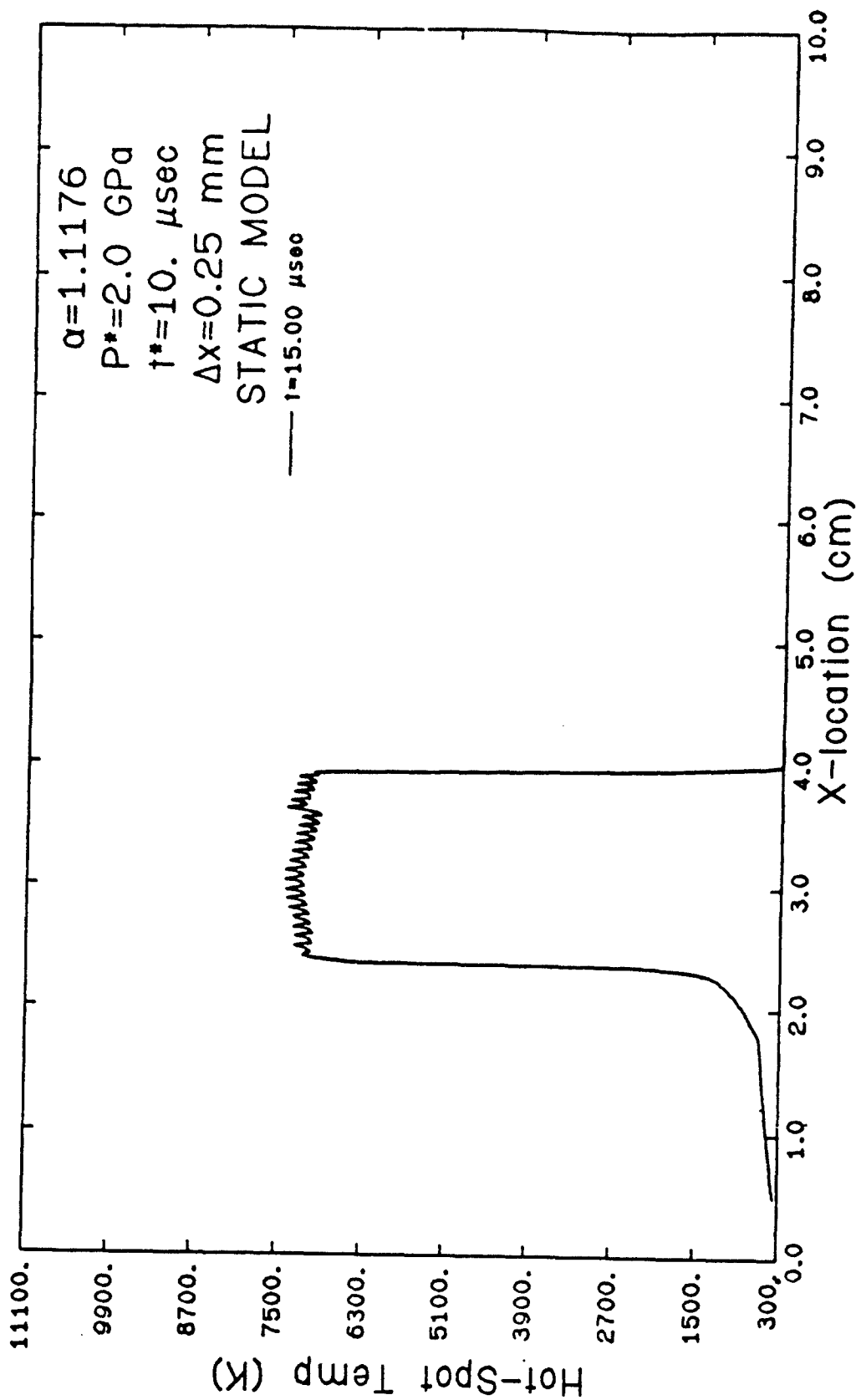Figure 23 Hot spot temperature profile in the explosive bed about 1.8 μsec after detonation using the reduced finite difference cell size of Δx = 0.25 mm. All other input data are identical to those of Figure 21.

51

Table 5 Effect of Timestep on Computed Results Using (a) The Dynamic Model and (b) The Static Model ($P^* = 2$ GPa, $t^* = 10$ μsec, $\alpha = 1.1176$, $a_0 = 39$ μm, $\Delta x = 0.25$ mm)

Run	Δt (nsec)	L_{SDT} (mm)	Deviation of L_{SDT} from Run 1	t_{SDT} (μsec)
1	5	23.0206	-----	13.22
2	4	20.5354	- 11%	13.224
3	6	22.5460	- 2%	13.158
4	10	21.2851	- 8%	12.54

(b)

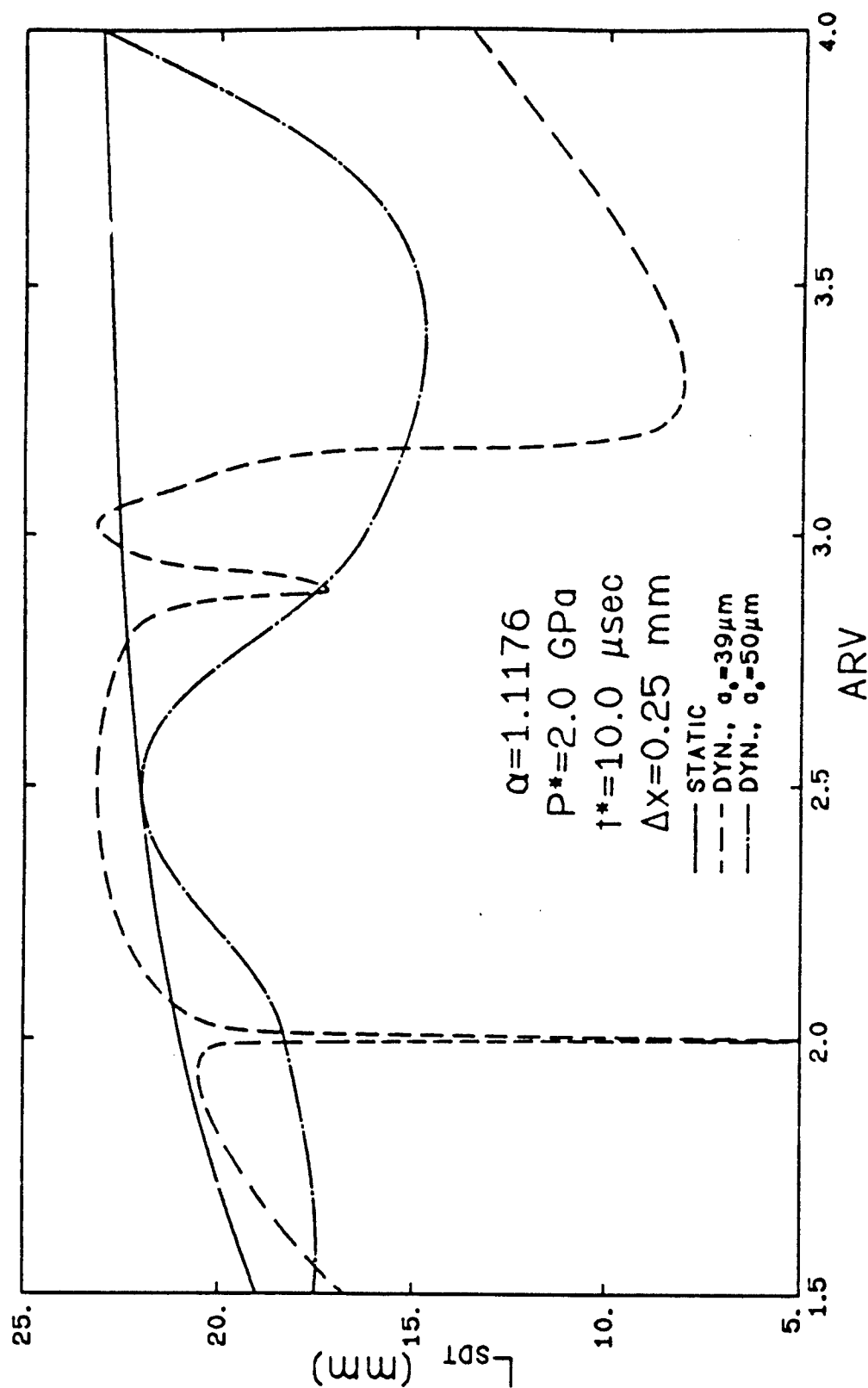| Run	Δt (nsec)	L_{SDT} (mm)	Deviation of L_{SDT} from Run 1	t_{SDT} (μsec)
1	5	22.5351	-----	13.13
2	4	22.5272	- 0.03%	13.116
3	6	22.5415	+ 0.03%	13.14
4	10	22.7974	+ 1.16%	13.26

(b)

Figure 24   Run-distance to detonation vs. the coefficient of
quadratic artificial viscosity showing results from
the dynamic model (for initial pore radii of 39 μm
and 50 μm) and the static model (independent of initial
pore radius). The erratic behavior of the dynamic results
is attributed to numerical difficulties.

"trouble spot" can be avoided simply by changing either Δx, Δt, ARV, or a_0 only slightly!

Finally, Figs. 25 and 26 give, respectively, dynamic and static hot spot temperature profiles for $\alpha = 1.5322$. Other input data, $P* = 2$ GPa, $t* = 10$ μsec, and $\Delta x = 0.5$ mm, is identical to that of Figs. 20 and 21 except that here a pore radius of 20 μm is used. Most noticeable is much lower values of the hot spot temperature for the more porous material. In addition, the oscillations in the dynamic curve are much smaller, fewer in number, and not as sharp as they were in Fig. 20 for the less porous material. The average value of the hot spot temperature appears to be about equal upon comparison of the static and dynamic results, whereas Figs. 20 and 21 ($\alpha = 1.1176$) show an 800 K difference in the average hot spot temperature between the two models.

In summary, a dynamic pore collapse model should be a more realistic representation of the actual compaction process. In the presentation here, however, certain combinations of ARV, Δx, and a_0 produce inexplainable "trouble spots" in which the run up distance and hot spot temperature profile deviate greatly from the expected trends. This is assumed to be a major fault in this dynamic model. These "trouble spots" are not found when using the static pore collapse model.

Dynamic Model Version 2: Kooker and Anderson [16]

This section briefly describes the dynamic pore collapse model of Kooker and Anderson [16] as well as how it was incorporated into our DSDT code. A comparison is then made of results from this model and Carroll and Holt's dynamic model.

The dynamic pore collapse relation of Kooker and Anderson [16] was written specifically for the modeling of hivelite solid propellant combustion. Their theory is similar to Carroll and Holt's [8] in that it is based on isolated pores or voids. They give the following time-dependent relation for α.

$$\frac{\eta_a}{\alpha(\alpha-1)} \frac{D}{Dt} (\alpha) = -P_{sm}(\rho_c, \alpha, e_c) + P_{eq}(\alpha, e_c) + P_{gas}(\alpha). \qquad (3.12)$$

This is the radial momentum equation through a hollow sphere, neglecting inertia. P_{sm} is the spherical stress in the solid matrix material, P_{gas} is the

Figure 25 Hot spot temperature profile in the explosive bed about
2.4 μsec after detonation. The dynamic model was used
along with an initial porosity of α = 1.5322 and an
initial pore radius of a_0 = 20 μm. All other input data
are identical to those of Figure 20 in which α = 1.1176
and a_0 = 39 μm. The numerical oscillations are less severe
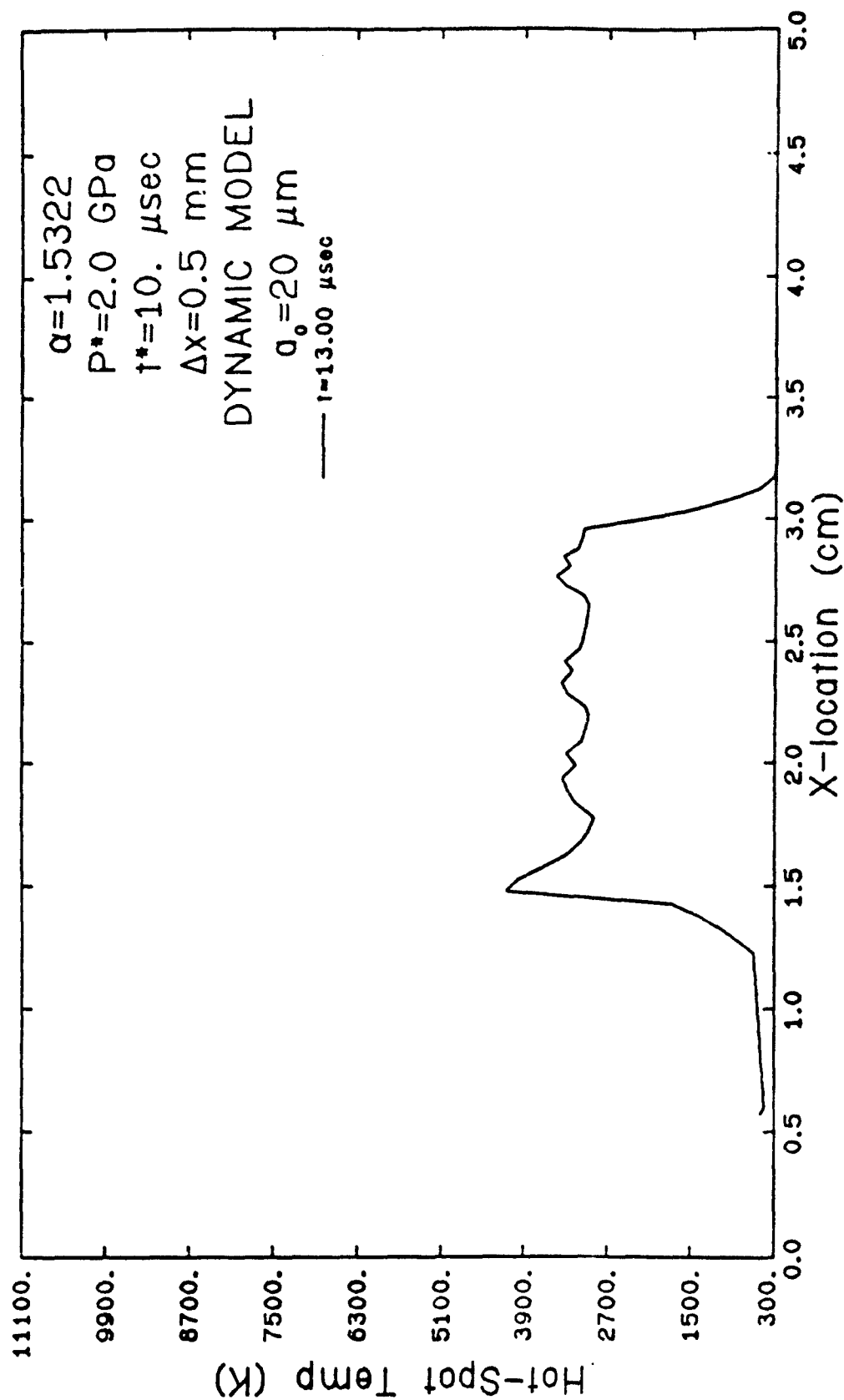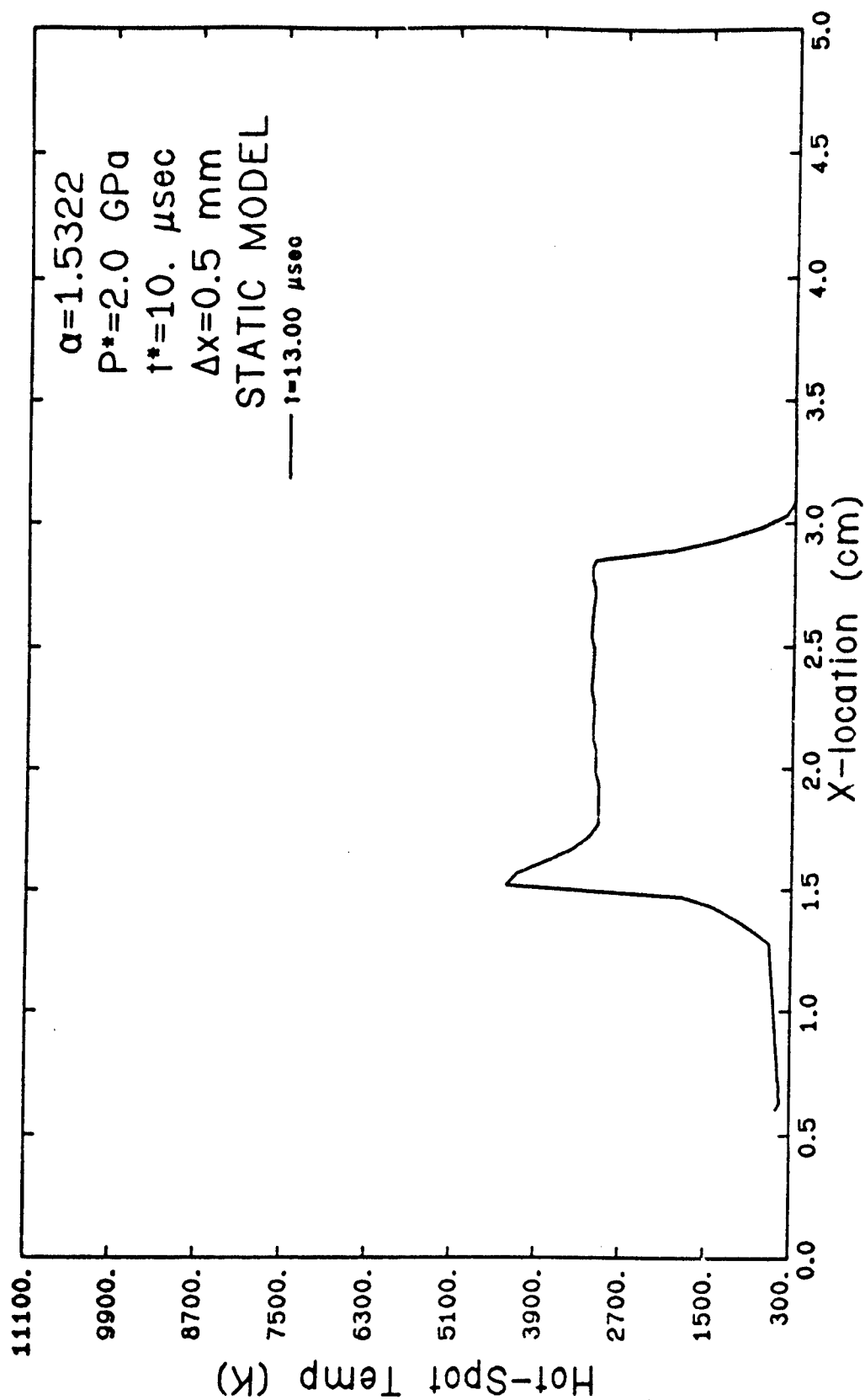for the more porous explosive.

Figure 26 Hot spot temperature profile in the explosive bed about 2.4 μsec after detonation. The static model was used along with an initial porosity of α = 1.5322. All other input data are identical to those of Figure 21.

pressure of the gas trapped in the pores, and P_{eq} is again the equilibrium stress field in the solid surrounding the pore. Also in Eq. (3.12), n_a is a viscosity type coefficient, ρ_c is the density of the condensed phase, and e_c is the internal energy of the condensed phase.

Different from Carroll and Holt's model, Kooker and Anderson's model does not involve separate phases of compression. They point out that while Carroll and Holt's model provides an excellent description for porous metals, it works poorly for solid propellant. Therefore, Kooker and Anderson present a different expression for $P_{eq}(\alpha, e_c)$, which is

$$P_{eq}(\alpha, e_c) = \tau_{eff}(\alpha, e_c) \ln (\frac{1}{\vartheta}) \qquad (3.13)$$

where

$$\tau_{eff}(\alpha, e_c) = \{\tau_0 + (\tau_1 - \tau_0)[1 - \varsigma^{P_1} - \tau^2(1 - \varsigma^{-1})]\} \cdot \{1 - (\frac{e_c - e_0}{e_{ml}})^2\} \qquad (3.14)$$

$$\varsigma \equiv \vartheta/\vartheta_0 \qquad \vartheta \equiv \frac{\alpha - 1}{\alpha}$$

τ_{eff} plays the role of a porosity-dependent yield stress. The multiplier involving internal energy in Eq. (3.14) provides for thermal softening, i.e. at the melting condition the material is unable to resist pore collapse. e_0 is the initial value of e_c, and e_{ml} is the melt energy of the condensed phase above e_0. The parameters $(\tau_0, \tau_1, \tau_2, P_1)$ in Eq. (3.14) are determined experimentally.

The following finite difference form of Eq. (3.12) was incorporated into Krier and Cudak's [1] code for the calculation of α at each timestep.

$$\alpha^{N+1} = \frac{\alpha^N(\alpha^N - 1)}{n_a} \{-P_{sm}^N + P_{eq}^N + P_{gas}^N\} \Delta + \alpha^N \qquad (3.15)$$

This relation is used throughout the entire compaction process. Note that since inertia is neglected, this equation is first-order (compare with that of Carroll and Holt, Eq. (3.11), which is second-order). The size of the timestep, Δ, is 5 nsec.

The use of this model requires values for the several parameters mentioned above. Since these values are not available for our explosive, HMX,

we are forced to use those values given by Kooker and Anderson for hivelite 1C86-8A, which are listed in Table 6. Even though the use of these values obviously will not give accurate numerical results for HMX, it is the intention here to at least incorporate the model in a working form into the code. Accurate values for those parameters listed in Table 6 are hoped to be obtained in the future for HMX.

Finally, keeping in mind the inaccuracies mentioned above, the results from this model will be compared to results from the Carroll and Holt model for a ramp wave input of $P^* = 2$ GPa, $t^* = 10$ μsec, an initial porosity of $\alpha_0 = 1.1176$, and a finite difference grid spacing of $\Delta x = 0.5$ mm. The comparison is summarized in Table 7. Examining this table, it is seen that while the run up distance given by Kooker and Anderson's model is 25 percent lower than the L_{SDT} from Carroll and Holt's model, the time to detonation given by the former is extremely high -- 142 percent higher than the t_{SDT} from Carroll and Holt's model.

A slightly modified version of Kooker and Anderson's model is also tested. This version ignores the multiplier involving internal energy on the right hand side of Eq. (3.14). That is, for this case,

$$\tau_{eff}(\alpha, e_c) = \tau_0 + (\tau_1 - \tau_0)[1 - \varsigma^{P_1} - \tau_2(1 - \varsigma^{-1})].$$ (3.16)

This run is made to see the effect of the thermal softening term on the computed results. It is also made since we are comparing these results to those using Carroll and Holt's model, which does not include such a term. However, we ran the code up to $t = 35$ μsec with no detonation occurring. This indeed demonstrates that with the thermal softening term, the resistance to pore collapse is weaker.

Table 6 Values for Parameters Used in Eq. (3.14) and (3.15)

Symbol	Value Assigned for Hivelite 1086-A [16]
n_a	3.44×10^5 dyne-sec/cm^2
e_o	2.54×10^{10} erg/g
e_{ml}	4.1023×10^9 erg/g
τ_o	0.0
τ_1	2.758×10^8 dyne/cm^2
τ_2	0.03 (non-dimensional)
P_1	4.0 (non-dimensional)

Table 7 Comparison of L_{SDT} and t_{SDT} using Two Different Dynamic Pore Collapse Models. The inputs are $p^* = 2$ GPa, $t^* = 10$ μsec, $\alpha_o = 1.1176$, $\Delta x = 0.5$ mm. For Carroll and Holt's [8] model, a pore radius of 20 μm was used.

	L_{SDT} (mm)	t_{SDT} (μsec)
Carroll and Holt	20.5032	12.4
Kooker and Anderson	15.3984	30.0
Difference	− 25%	+ 142%

REFERENCES

1. Krier, H. and Cudak, C. A., Technical Report No. UILU-ENG-84-4007; Department of Mechanical and Industrial Engineering, University of Illinois at Urbana-Champaign, September 1984.

2. Butler, P. B., Lembeck, M. L., and Krier, H., "Modeling of Shock Development and Transition to Detonation Initiated by Burning in Porous Propellant Beds," Combustion and Flame, 46 (1982), 75-93.

3. Butler, P. B., and Krier, H., "Analysis of Deflagration to Shock to Detonation Transition (DSDT) in Porous Energetic Solid Propellants," AGARD Conference Preprint No. 367, paper No. 5, Lisse, The Netherlands, 1984.

4. Butler, P. B., and Krier, H., "Analysis of Deflagration to Detonation Transition in High-Energy Solid Propellants," to appear, Combustion and Flame, 1985.

5. Bernecker, R. R., "The DDT Process for High Energy Propellants," AGARD Conference Preprint No. 367, paper No. 14, Lisse, The Netherlands, 1984.

6. Price, D., and Bernecker, R. R., "Sensitivity of Porous Explosives to Transition from Deflagration to Detonation," Combustion and Flame, 25 (1975) 91-100.

7. Setchell, R. E., "Effects of Precursor Waves in Shock Initiation of Granular Explosives," Combustion and Flame, 54 (1983), 171-182.

8. Carroll, M. M., and Holt, A. C., "Static and Dynamic Pore-Collapse Relations for Ductile Porous Materials," J. Appl. Physics, 43:4 (1972), 1627-1636.

9. Hayes, D. B., "Shock Induced Hot-Spot Formation and Subsequent Decomposition in Granular, Porous, Hexanitrostiblene Explosive," Detonation Physics Symposium, Minsk, Russia, 1981.

10. Baer, M. R., and Nunziato, J. W., "A Theory for Deflagration-to-Detonation Transition (DDT) in Granular Explosives," SAND Report, SAND82-0293, 1983.

11. Cowperthwaite, M., and Zwisler, W. H., "TIGER" Computer Code Documentation," Rept. PYU-1281, Stanford Research Institute, 1974.

12. Coyne, D.W., Butler, P. B., and Krier, H., "Shock Development From Compression Waves Due to Confined Burning in Porous Solid Propellants and Explosives," AIAA Paper No. 83-0480, Reno, Nevada, 1983.

13. Dick, J. J., "Measurement of the Shock Initiation Sensitivity of Low Density HMX," Combustion and Flame, 54 (1983), 121-129.

14. Lindstrom, I. E., "Planar Shock Initiation of Porous Tetryl," J. Applied Physics, 43:1, January 1970, 337-350.

15. Sandusky, H. W., and Bernecker, R. R., "Compressive Reaction in Porous Beds of Energetic Materials," Proceedings of Eighth Symposium (International) on Detonation, Albuquerque, New Mexico, July 1985, 631-640.

16. Kooker, D. E., and Anderson, R. D., "Modeling of Hivelite Solid Propellant Combustion," Technical Report BRL-TR-2649, U. S. Army Ballistic Research Laboratory, Aberdeen Proving Ground, Maryland, April 1985.

Blank Page